DM3-ABY4

Design, Analysis, and Testing of an Electromagnetic Booster Separation System

A Major Qualifying Project Report
Submitted to the Faculty of the
WORCESTER POLYTECHNIC INSTITUTE
in Partial Fulfillment of the Requirements for the
Degree of Bachelor of Science
in Physics

by

Justin Tavares

April 25, 2019

Approved by: _____
David C. Medich, Advisor
Associate Professor, Physics Program
WPI

Abstract

This paper describes a project to design, analyze, and test an electromagnetic booster separation system for a high-powered model rocket. A first-principles model was derived for the system using magnetic theory for permanent magnets, electromagnetic theory of real finite coils, and circuit theory for a LRC discharge circuit. A prototype system for the coil and circuit was fabricated and tested, and the resulting design was found to successfully minimize the capacitance required, reducing the overall system mass. A finite element analysis was conducted to further prove the derived physics-based model. Results of this analysis and testing are presented, and recommendations for future work are given.

Acknowledgements

I would like to thank the following individuals and groups for their help and support throughout the entirety of this project.

- Project advisor Professor Medich for graciously supporting my MQP project idea midway through senior year
- Professor Blandino and Professor Jayachandran for their guidance with MQP paper writing
- Design of a High-Powered Model Rocket MSAT, Controls, and PSR MQP teams for their work on integration of the electromagnetic booster separation design into the SPACEJAM rocket
- The WARRIORS I MQP for providing me with a foundation for my MQP
- Nicholas Lucena for generously donating leftover supplies from the AE MQP lab and for assistance with circuit testing

Table of Contents

List of Figures

Chapter 1: Introduction

The investigation of model rocketry has become more popular among many aerospace engineering departments at universities across the United States. These projects allow students to gain experience in rocket propulsion, staging, separation, recovery, stability, and control which are considerations also applied by professional rocket engineers. WPI has undertaken four MQP model rocket projects over the last decade to investigate the academic merit of these projects with an emphasis of analysis normally not achieved in the hobby model rocketry community. These projects have innovated model rocketry systems and mechanisms by applying fundamental physics principles to rocket science. Among these model systems analyzed and tested in flight is the electromagnetic booster separation system, which has been studied by three of the four past model rocket MQP projects at WPI. [1][2][3] This parallel stage separation technique is innovative and has shown promising results because of its safety during flight and repeatability for ground testing not achievable by traditional pyrotechnic separation techniques. In addition, this system relies on many advanced principles of magnetic, electromagnetic, and series circuit theory, and so has provided a rewarding and rigorous academic exercise for the previous rocket MQP teams.

However, there have been several barriers and limitations that previous rocket MQP teams have faced when attempting to implement this system into their model rocket. At this point, no team has successfully separated all of the rocket boosters despite successful ground tests. I hypothesized that this lack of success was caused by limitations in the supporting physics background used to create the system. These limitations include (1) assumptions and approximations that are too great to be negligible in practice, (2) elements of the proposed physical model that may have been incorrect, (3) applying safety factors and overcompensating in circuit power just to have successful ground tests without analyzing the physics model for errors. As a result, previous teams were not able to make extensive evidence to support the theory that they derived and simply wanted to have a successful ground test. It would be highly beneficial, therefore, for this system to be analyzed and tested through methods such as finite element analysis (FEA) simulations and detailed circuit testing to prove the fundamental physics model that is be used for the system.

The goal of this project is to develop a more accurate physics-based model for the electromagnetic booster system. This model will be based on the models derived from previous MQP teams and also will consider the magnetic field strength and forces between permanent

magnets and ferromagnetic materials. Furthermore, a more detailed and accurate model for the inductance of a finite electromagnet coil will be derived which will include with the effects that multiple ferromagnetic cores have on stage separation; , this model will emphasize corrections for phenomena such as magnetic field leakage, self-inductance, and mutual inductance of a coil. I also will conduct a detailed analysis and testing of this physics-based model through COMSOL Multiphysics® simulations and through circuit testing and curve fitting analysis. [4] Another goal of this project is to write a project report that future model rocketry MQP teams can refer to if they wish to implement an electromagnetic booster separation system into their rocket design. The style of the report would be to provide a detailed derivation of the physics-based model, as well as convincing results from extensive analysis and testing so that future teams are confident with using these results to create their own system. This will be particularly useful for Aerospace Engineering majors that do not have the adequate Physics and Electrical Engineering (ECE) background required for the analysis that is necessary for designing this system. The report will include the essential equations, methodology, and MATLAB code required to size and fabricate their own electromagnetic actuators to use in their system. With this project, future model rocketry projects (such as the WPI high-powered model rocket MQP confirmed for the 2019-2020 academic year) will be able to more confidently and efficiently implement an electromagnetic booster separation system into their rocket design.

Chapter 2: Background

2.1 Rocket Staging and Separation Mechanisms

A multistage rocket is designed to carry a payload from the earth's surface into outer space using two or more rocket stages. Each stage contains an airframe, motor, and propellant. As a stage runs out of propellent, it is jettisoned, thereby reducing the overall rocket mass and allowing the thrust of future stages to better accelerate the rocket. As shown in Eq. (1), the classical rocket equation (which considers only gravitation forces) shows that the total change in velocity increases as the final "dry mass" decreases. [5]

$$\Delta v = v_e \ln \frac{m_0}{m_f} \tag{1}$$

Here, Δv is the maximum change in velocity of the rocket with no external forces, v_e is the effective exhaust velocity, m_0 is the initial total mass, and m_f is the final dry mass. This means that the maximum achievable altitude also will increase with greater burnout velocity since the change in altitude is proportional to the square of the burnout velocity. [5]

Rocket staging is categorized into two different forms: parallel and series. [5] Series staging is the more popular staging method in model rocketry. In this type of staging, the payload of the first stage is essentially another model rocket, consisting of its own airframe structure and motor. Once the first stage motor propellant has been exhausted, a mechanism must then separate this stage from the payload (second stage) and ignite the second stage motors. A diagram showing a typical series staging process is shown in Figure 1. On the contrary, in parallel staging all of the stage motors all ignited on the launch pad at the same time so that all stages are operating at once. The stage motors and airframes are quite properly called "boosters" and the main payload (the center airframe) is the core or the sustainer. Both the boosters and core airframe have motors, but the booster motors are selected to have less duration than the core airframe motor so that the core airframe can still produce thrust after the boosters have been separated. A diagram showing a typical parallel staging process is shown in Figure 2. Parallel staging is less commonly used in the model rocketry community because of the issue of "clustering" multiple motors. Using multiple or clustered motors runs the risk of not igniting all motors on the launch pad at the same time. This

non-simultaneous ignition has many dangers during launch, as non-symmetric thrust will create torque that steers the rocket away from the desired vertical trajectory. [5] Because of this risk, there hasn't been much activity or research in parallel staging for model rockets. Therefore, there is academic merit in investigating parallel staging, as well non-conventional separation mechanisms.

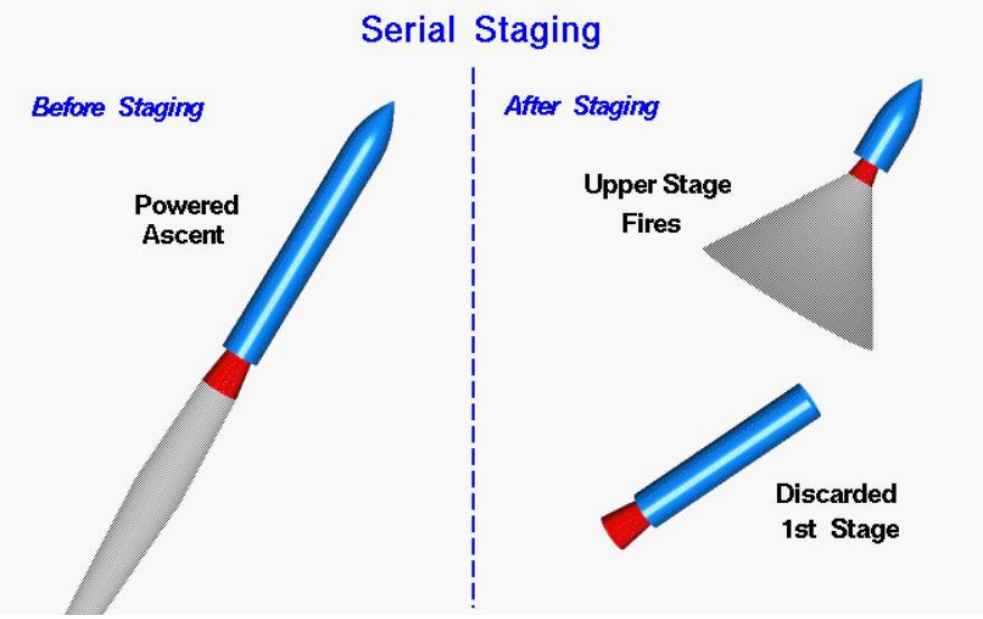

Figure 1. Serial staging diagram. [6]

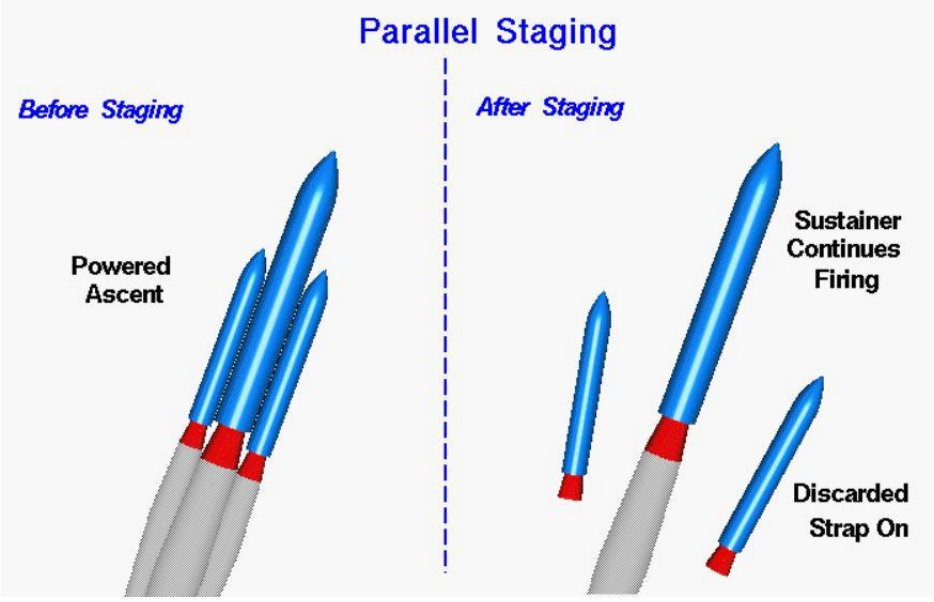

Figure 2. Parallel staging diagram. [6]

Typical separation mechanisms use a black powder ejection charge, which is a small grain of gunpowder installed at the end of a delay grain in the rocket motor. [5] A diagram of a typical model rocket motor is shown in Figure 3. The delay grain produces no thrust when burned and allows the rocket to travel upward after the propellant is completely used up. The delay grain is modified for the core motor to allow for a delay time that would let the final rocket stage travel to apogee, the highest point of the trajectory, before the flame reaches the ejection charge. When the delay grain is completely consumed and the flame reaches the black powder charge, the charge is ignited to release hot gas into the rocket airframe. Black powder has a similar composition to gunpowder and when ignited, generates hot gases that pressurize the rocket's airframe. The buildup of hot gas in the airframe increases the internal pressure enough to pop the nose cone off the top of the rocket and deploy the recovery device. The black powder ejection charge is an example of a "pyrotechnic" separating mechanism because it relies on ignition and combustion of black powder to cause separation. Pyrotechnic methods of separation are widely used for model rockets, however, there are some downsides. Because pyrotechnic methods require a flame to combust the black powder, there is a risk of scorching airframe parts and even causing the airframe to catch fire. In addition, it can be dangerous to conduct extensive ground testing of pyrotechnic mechanisms because of the large amount of hot gas released once the nose cone is ejected. Furthermore, pyrotechnic separation is widely used and therefore does not offer much academic merit for further analysis and testing. For these reasons, there are benefits for establishing a new mechanism for stage separation.

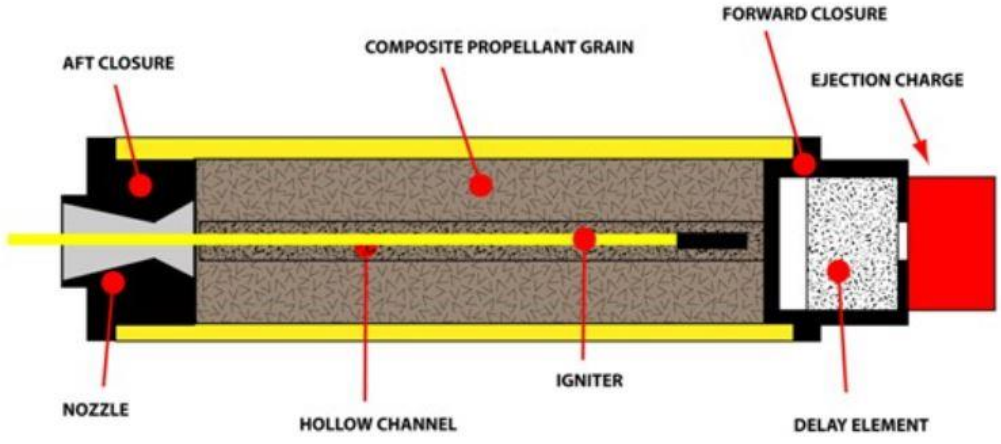

Figure 3. Composite rocket motor diagram. [7]

2.2 Electromagnetic booster separation

Electromagnetic booster separation is a kind of rocket separation system in which the side boosters are ejected from the main airframe using an electromagnetic actuator. The WARRIORS I MQP from 2005, WARRIORS II MQP from 2006, and SPACEJAM MQP from 2019 each used electromagnetic booster separation as an innovative parallel staging technique using a non-pyrotechnic separation mechanism. [1][2][3] These projects advanced electromagnetic booster research yet, each has had their own barriers and inconsistencies in analysis and testing. In this MQP project, we used a permanent magnet located within the rocket's booster engine to induce stage separation.. A diagram illustrating the electromagnet and permanent magnet connection is shown in Figure 4. The permanent magnet and electromagnet are sized so that there is a large enough magnetic force to hold the boosters to the rocket airframe during the launch phase. Once the booster motors have exhausted all of their propellant, an on-board computer sends a signal to an LRC circuit connected to the electromagnets. The signal discharges the LRC circuit capacitors thereby creating a high amplitude current-pulse that flows through the LRC electromagnet. This pulse therefore will create a strong magnetic field that opposes the magnetic field of the permanent magnet, resulting in separation of the boosters from the rocket airframe. The LRC circuit must be designed to produce a high enough current through the electromagnet, and the electromagnet must be designed to maximize the magnetic field produced within the spatial limitations of the motor section.

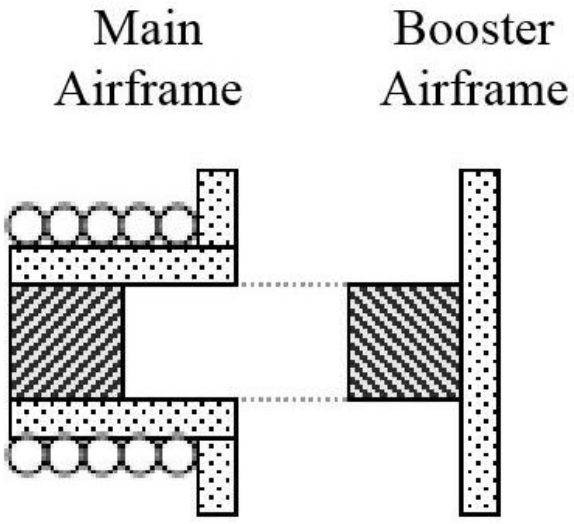

Figure 4. Electromagnetic actuator connection. [3]

2.3 Rocket booster forces

There are several forces that act on a rocket booster while attached to the airframe during flight. These forces can be divided into two types: axial and radial. The primary axial force is the downflow drag force. Drag is the force acting opposite to the relative motion of any object moving with respect to a surrounding fluid. The "downflow" drag force is the axial drag force specifically on the booster cross-section, which can be calculated using Eq. (2),

$$F_d = \frac{1}{2}\rho v^2 C_d A \tag{2}$$

where F_d is the downflow drag force, ρ is the average atmospheric density, v is the maximum estimated velocity, C_d is the drag coefficient of the rocket, and A is the cross-sectional area of the booster. An estimate of the drag coefficient can be obtained from OpenRocket, a rocket motion simulation software, given a basic geometry of the rocket airframe, cone, and boosters. As an example, OpenRocket calculated the drag coefficient for our SPACEJAM rocket to be approximately 0.7, which is roughly equal to typical drag coefficients of model rockets tested in wind tunnels. The OpenRocket simulator geometry for the SPACEJAM rocket is given in Appendix A. The cross-sectional area of the booster airframe is primarily dependent on the diameter of the motor being used. For lower-powered composite propellant motors, such as F-level motors, the diameter may be as wide as 29mm in diameter. An example of typical F-level rocket motor statistics are given in Appendix B. [8]

Radial forces include radial drag, also called asymmetric drag, and the centrifugal forces caused from spinning during flight. Drag is the force acting opposite to the relative motion of any object moving with respect to a surrounding fluid. Although the relative motion of the rocket is upwards, there is a component of the downstream drag force after the nose cone in the radial direction that is caused by the deflection of atmosphere around the nose cone. This force can be approximated at 10% of the axial drag force calculated from Eq. (2). The other radial force is the centrifugal force outwards radially due to the rocket's spin. Using the conventional yaw, pitch, roll body-fixed coordinate system for aircrafts, as shown in Figure 5, the rocket spin occurs in the roll direction and is created by fluid flow over fins located at the bottom of the rocket, which are

commonly used by both model and some real-scale rockets to allow for spin stability in the Earth's atmosphere.

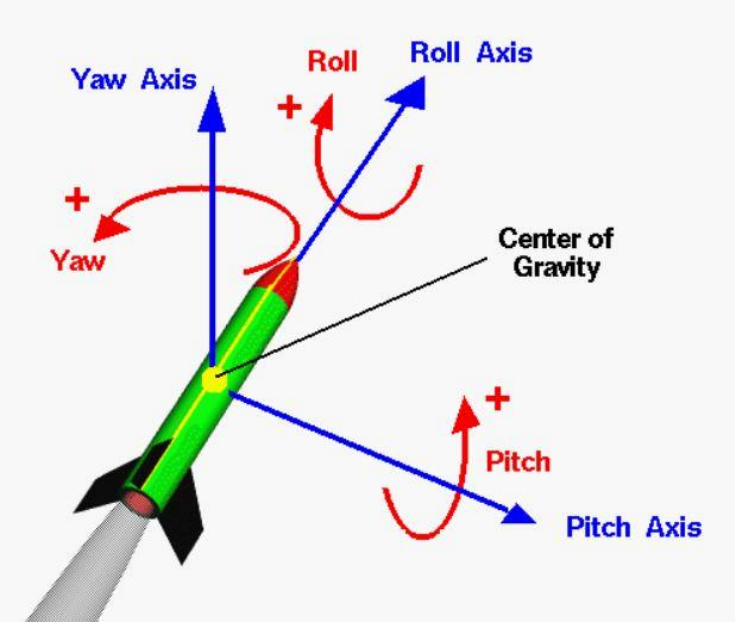

Figure 5. Yaw, pitch, roll body-fixed coordinate system. [9]

For a rocket to be stable in flight, the rocket requires a high enough "roll rate," or angular speed, to help the rocket from steering off the desired vertical trajectory. It is difficult to determine what corresponding roll rate is generated by a certain fin shape and configuration; however, experimental data shows that a rocket needs a minimum roll rate of 1 Hz to be spin stabilized, which is easily achievable by most fin designs. However, some model rockets have achieved a roll rate of up to 10 Hz from their fins. The centrifugal force due to the rocket spin can be calculated according to Eq. (5).

$$F_c = \omega^2 r m_b \tag{5}$$

where F_c is the centrifugal force, ω is the angular roll rate, and r is the distance between the airframe and booster center axes. For the purposes of electromagnetic booster separation, the ideal fins generate a high enough roll rate to allow for spin stability but a low enough roll rate so the

centrifugal force on the booster is not too great, since a lower net outward radial force on the booster allows for a smaller permanent magnet to be used to hold the booster to the rocket airframe.

2.4 Magnetic Theory of Permanent Magnets

When matter is placed in a magnetic field, , the field induces tiny magnetic dipoles in the material with a net alignment either parallel or antiparallel to the direction of the magnetic field. There are several ways in which a material can become magnetized. Paramagnetic materials are ones in which magnetism is induced parallel to the magnetic field while diamagnetic materials have induced magnetic fields that are opposite (antiparallel) to the magnetic field. In both paramagnetic and diamagnetic materials, the induced magnetization within the material is sustained by the field and disappears when the material is removed from the magnetic field. Alternatively, ferromagnetic materials retain their magnetization even after the external field has been removed. This occurs because the magnetic dipoles in ferromagnetic materials are "prone" to point in the same direction as neighboring dipoles. A group of dipoles aligning in the same direction are referred to as domains. With increased magnetic field, the size and number of domains parallel to the magnetic field grows until the material reaches its saturation point, at which all dipoles point in the same direction that are parallel to the magnetic field. When the magnetic field is turned off, some domains that return to randomly oriented domains, but many will remain in the direction that was parallel to the magnetic field resulting in a permanent magnetic field. A permanent magnet can now, in turn, adjust and thereby magnetize the molecular magnets in other ferromagnetic material. An example of inducing a permanent magnetic field can be shown by rubbing a permanent magnet with ferromagnetic iron: While the iron initially does not have a magnetic field, as it is exposed to the magnet's field, the magnet aligns the domains in the iron with its field causing the iron to permanently have a magnetic field. [10]

Just as non-magnetic ferromagnetic materials can be magnetized, magnetized ferromagnetic materials also can be demagnetized. For the ferromagnetic material to be demagnetized, it must be exposed to a strong magnetic field in the opposite direction or heated to high temperature to cause the domains to become random again. If an alternating magnetic field is applied to the material, its magnetization will trace out a loop called a hysteresis loop. This lack of retraceability of the magnetization curve is caused by the dependence of the state of the system

on its history, a the property called hysteresis. For magnetism, hysteresis is caused by the existence of previous magnetic domains in a magnetic material. [10] The relationship between the magnetic field and the magnetization of a material can be expressed in terms of the auxiliary field $\boldsymbol{H}$, defined in Eq. (6), [10]

$$\boldsymbol{H} = \frac{1}{\mu_0}\boldsymbol{B} - \boldsymbol{M} \tag{6}$$

where $\boldsymbol{B}$ is the magnetic field strength and $\boldsymbol{M}$ is the magnetization. Then, the magnetization can be expressed in terms of $\boldsymbol{H}$ according to Eq. (7), [10]

$$\boldsymbol{M} = \chi_m \boldsymbol{H} \tag{7}$$

where χ_m is the magnetic susceptibility, a dimensionless material property. Materials that obey this equation are called linear media, and the magnetic field corresponding to this magnetization can be expressed according to Eq. (8), [10]

$$\boldsymbol{B} = \mu \boldsymbol{H} \tag{8}$$

where μ is the permeability of the material and can be defined according to Eq. (9), [10]

$$\mu = \mu_0(1 + \chi_m) \tag{9}$$

where μ_0 is the permeability of free space. If a vacuum is assumed, the susceptibility vanishes and the permeability is simply μ_0. [10]

The force between two ferromagnetic materials is a complicated function of the magnetic field distribution, geometry, and distance between the materials. [10] These models depend on whether or not the distance between the magnets is much greater or less than the size of the magnets. In case of a homogeneous magnetization, the problem can be simplified using the

Divergence theorem. The Divergence theorem, shown in Eq. (10), relates the surface integral contributions of a field to its volumetric elements, [11]

$$\iiint \nabla \cdot \boldsymbol{M} dV = \oiint \boldsymbol{M} \cdot \hat{\boldsymbol{n}} dS \tag{10}$$

Here, $\hat{\boldsymbol{n}}$ is the outward normal from the magnets surface. Upon integration of the magnetization, all dipoles along the surface of integration cancel each other, except at the magnet's end surfaces. The field then emerges only from those "magnetic charges" spread over the magnet's end facets. If the magnet also has flat end facets, such as a cylinder or prism, then the surface charge distribution at the end faces is also uniform. This simplification is known as the Gilbert model. The force on the flat surface of two nearby magnetized objects then is derived from the potential energy of the corresponding magnetic field at the magnet end faces. this magnetic potential energy is calculated using Eq. (11), [10]

$$U = \frac{1}{2} \iiint \frac{1}{\mu_0} B^2 \, dV = \frac{1}{2} \iiint \frac{1}{\mu_0} B^2 \, dA_m \, dz = \frac{z B_z^2 A_m}{2\mu_0} \tag{11}$$

Here, V is the volume of the region between two magnetized objects, A_m is the area of the end face of the magnet and z is the distance between the end faces of the magnetized objects. The magnetic force between the two magnetized objects is the force normal to the magnet end face and is derived from Eq. (12)

$$F_z = -\frac{dU}{dz} = -\frac{B_z^2 A_m}{2\mu_0} \tag{12}$$

where the negative sign indicates that the force is attractive if the magnetic field lines point outward from the end face. When two magnets or a magnet and ferromagnetic object are attached through this force, the force is the adhesive force. The adhesive force is perpendicular to the magnet surface, but this also creates a force parallel to the surface if a shear force was applied to the system. The combined vector sum of the adhesive and parallel force strength is often called the "holding strength." The parallel component of the holding strength is a function of the adhesive force and

the friction between the two surfaces. This relationship is difficult to quantify, but it can be approximated that the parallel component is between 15-25% of the adhesive strength for most materials. [12]

To use the equation for the adhesive force between two magnetized surfaces, we must also know the magnetic flux density $\boldsymbol{B}$ at the surface of the magnet. This is often only possible using numerical methods, but analytical solutions are available for more basic permanent magnet geometries, such as a cylinder. The magnetic scalar potential of a dipole as a function of its distance from the dipole center is given by Eq. (13). [13]

$$\Phi_{dipole}(\boldsymbol{x}) = \frac{1}{4\pi}\frac{\boldsymbol{m}\cdot\hat{\boldsymbol{n}}}{|\boldsymbol{x}^2|} \tag{13}$$

If we take a differential magnetic dipole dm in the permanent magnet as shown in Figure 6a, then the differential magnetic potential along the z-axis is given by Eq. (14).

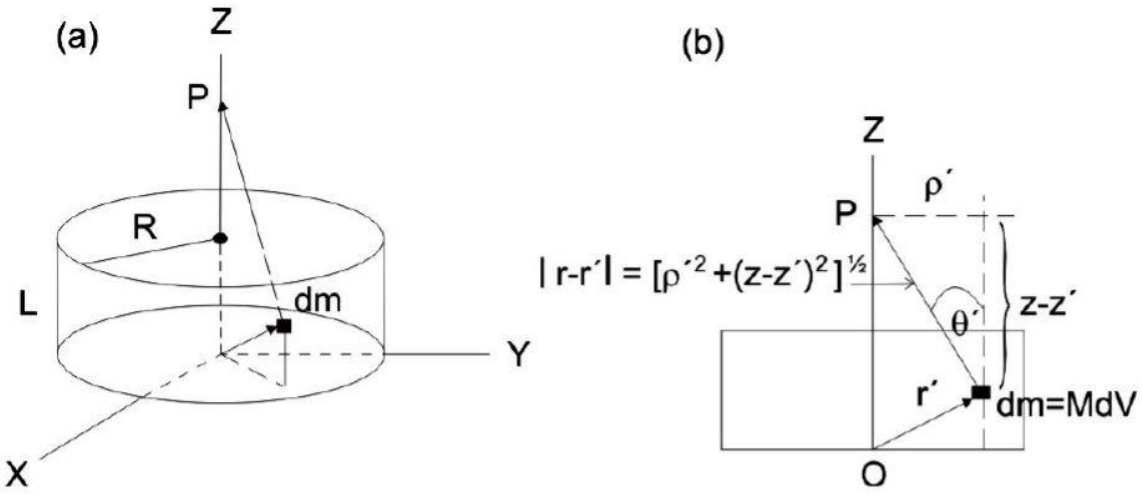

Figure 6. (a) Schematic of cylindrical magnet.
(b). Geometry of differential magnetic dipole segment. [13]

$$d\Phi_{axis} = \frac{1}{4\pi}\frac{dm\cos\theta'}{|\boldsymbol{r}-\boldsymbol{r}'|^2} \tag{14}$$

The differential magnetic dipole dm can be expressed in terms of the magnetization M using Eq. (15), which allows the differential volume to be expressed in terms of the cylindrical coordinate differential components.

$$dm = MdV = M\rho' d\rho' d\varphi' dz' \tag{15}$$

Then, $\cos\theta'$, the distance $\boldsymbol{r}$, and the distance $\boldsymbol{r'}$ can be substituted in terms of cylindrical coordinates, as illustrated in Figure 6b, according to Eq. (16),

$$d\Phi_{axis} = \frac{M}{4\pi} \frac{z - z'}{[(z - z')^2 + \rho'^2]^{\frac{3}{2}}} \rho' d\rho' d\varphi' dz' \tag{16}$$

The differential magnetic potential can then be integrated along the volume of the cylinder according to the triple integral in cylindrical coordinates given in Eq. (17).

$$\Phi_{axis}(z) = \frac{M}{4\pi} \int_0^{2\pi} d\varphi' \int_0^{L_m} (z - z') dz' \int_0^{R_m} \frac{\rho' d\rho'}{[(z - z')^2 + \rho'^2]^{\frac{3}{2}}} \tag{17}$$

After evaluating the triple integral along the cylinder volume, the resulting scalar potential in the z-axis is given in Eq. (18).

$$\Phi_{axis}(z) = \frac{M}{2}\left(\sqrt{(z - L_m)^2 + R_m^2} - \sqrt{z^2 + R_m^2}\right) \tag{18}$$

Using the following relationship between the scalar magnetic potential and the magnetic flux density, the magnetic flux density along the z-axis is then finally derived in Eq. (19).

$$B_z(z) = \mu_0 \frac{d\Phi_{axis}}{dz} = \frac{\mu_0 M}{2}\left(\frac{z}{\sqrt{z^2 + R_m^2}} - \frac{z - L}{\sqrt{(z - L_m)^2 + R_m^2}}\right) \tag{19}$$

Then, substituting z = 0 into this equation and replacing $\mu_0 M$ with the residual magnetism B_r will give the magnetic flux density at an end surface according to Eq. (20). [13]

$$B_z(z) = \frac{B_r}{2} \frac{L_m}{\sqrt{L_m^2 + R_m^2}} \tag{20}$$

2.5 Electromagnetic Theory of a Coil

An electromagnet is a device that creates a magnetic field by running a current through a conductor. Ampere's law says that the integral of the magnetic field strength B around any closed loop of the field is equal to the sum of the current flowing through the loop and is given in Eq. (21). [10]

$$\oint \boldsymbol{B} \cdot d\boldsymbol{l} = \mu_0 I_{enc} \tag{21}$$

While Ampere's law can only be used under conditions of high-symmetry, the Biot-Savart law, given in Eq. (22), is a generalized equation that is used to calculate the strength of the magnetic field due to a particular segment of current in the overall wire. [10]

$$\boldsymbol{B}(\boldsymbol{r}) = \frac{\mu_0}{4\pi} \int \frac{\boldsymbol{I} \times \hat{\boldsymbol{r}}}{r^2} dl' = \frac{\mu_0 I}{4\pi} \int \frac{d\boldsymbol{l}' \times \hat{\boldsymbol{r}}}{r^2} \tag{22}$$

The direction of the generated magnetic field is determined by the right-hand rule, which states that if the fingers of the right hand are pointed in the direction of current flow, then the thumb points in the direction of the magnetic field. A visualization of this rule for a coil is given in Figure 7.

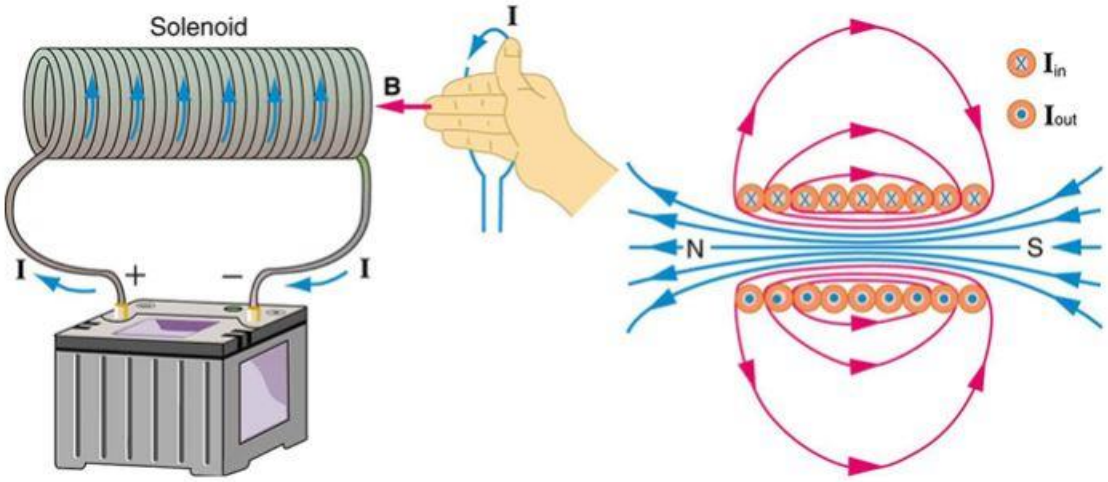

Figure 7. Magnetic field produced by solenoid coil current right hand rule. [14]

A solenoid coil is a common type of electromagnet formed when a conducting wire is wrapped in a helix shape for a specified number of turns. Following the right-hand rule, this creates a magnetic field that points essentially parallel to the axis of the coil towards the axial direction of current flow. Many solenoid coil electromagnets make use of a cylindrical ferromagnetic core to amplify the magnetic field strength that is produced. The current through the coil magnetizes the ferromagnetic core, and the field of the magnetized core adds to the field produced by the wire. Using a ferromagnetic core can increase the magnetic field of a coil by hundreds or thousands of times over what it would be without the core. A coil with a core which forms a closed loop is called a closed-core coil. By providing a closed path for the magnetic field lines, this geometry minimizes the magnetic reluctance and produces the strongest magnetic field. By using a ferromagnetic core, the permeability of the coil, μ, is calculated by multiplying the permeability of free space, μ_0, by the relative permeability of the material, μ_r, as shown in Eq. (23) [10]

$$\mu = \mu_r \mu_0 \tag{23}$$

where the relative permeability μ_r is an intrinsic property of magnetic and ferromagnetic materials. A closed path in a coil can be achieved by using a core that spans the entire length of the coil so that there are no "gaps" in the inside of the coil. If there are "air gaps" inside an infinite coil, then Ampere's law has to be modified according to Eq. (24). [15]

$$NI = B\left(\frac{L_{core}}{\mu} + \frac{L_{gap}}{\mu_0}\right) \tag{24}$$

If multiple different ferromagnetic materials are used, such as both a ferromagnetic core and a permanent magnet of different relative permeabilities, then Ampere's law can be modified to Eq. (25). [15]

$$NI = B\left(\frac{L_{core,1}}{\mu_1} + \frac{L_{core,2}}{\mu_2}\right) \tag{25}$$

Inductance in a characteristic of an electrical inductor, such as a coil, which indicates how resistive the device is to a change in the current. The greater the inductance of a device, the harder it is to change the current flowing through it. This is because a change in current will induce a reverse electromotive force (emf) in the opposite direction of the current change, as given by Faraday's law and presented in Eq. (26). [15]

$$\varepsilon = -L\frac{dI}{dt} \tag{26}$$

Here, L is the inductance and $\frac{dI}{dt}$ is the rate of change in the current. This is particularly useful when an electromagnet is incorporated into an electrical circuit. Using Faraday's law, the voltage across an inductor, which has the same magnitude as the emf generated in the inductor during a change in current, can be calculated according to Eq. (26). Therefore, the inductance L is an important parameter to know if the particular solution for a circuit is required for analysis. A useful simplification of the electromagnet coil problem is to assume an infinite coil so that the magnetic field lines inside the coil are assumed to be parallel to the coil axis. In this case, Ampere's law is simplified so that the magnetic field strength of an infinite coil can be determined by Eq. (27). [10]

$$B = \frac{\mu NI}{L} \tag{27}$$

In addition, the inductance of an infinite coil is a useful approximation for many cases using electromagnets in circuits. For a fixed cross-sectional area of an electromagnet and a changing current, Faraday's law reduces to Eq. (28). [10]

$$\varepsilon = -NA\frac{dB}{dt} = -\frac{-\mu N^2 A}{L}\frac{dI}{dt} \tag{28}$$

Using Eq. (26) and Eq. (28), respectively, solving for the inductance L for an infinite solenoid coil gives Eq. (29).

$$L = \frac{\mu N^2 A}{L} \tag{29}$$

However, this simplification does not consider the magnetic field strength near the ends of the real coil, which vary significantly from the magnetic field strength in the center of an infinite coil. Therefore, it is necessary to derive a solution for the magnetic field strength along the centerline (z-axis) of a finite length as a function of z, where the origin is centered at half the coil length. The diagram for this derivation is given in Figure 8.

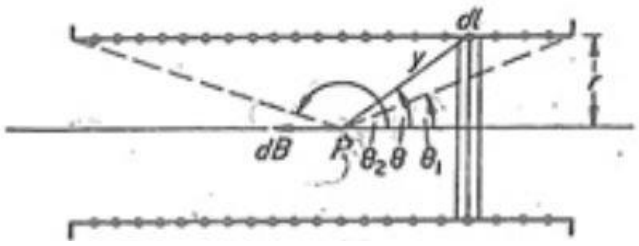

Figure 8. Magnetic field produced by differential coil length element. [16]

The axial (z-axis) magnetic field at a certain location inside a finite coil of known radius and length at a certain point inside the coil is given by Eq. (30). [17]

$$B = \frac{\mu NI}{2}\int_{\theta_1}^{\theta_2} \sin\theta \, d\theta \tag{30}$$

For a point along the centerline in the exact middle of the coil, according to the geometry of the Figure 8, the radius and length of the coil are related to θ_1 and θ_2 according to Eq. (31).

$$\cos\theta_1 = \cos\theta_2 = \cos\left(\tan^{-1}\frac{2R}{L}\right) \tag{31}$$

From the following trigonometric identity, shown in Eq. (32), Eq. (30) can be integrated and simplified to give Eq. (33).

$$\cos(\tan^{-1}(x)) = \frac{1}{\sqrt{x^2+1}} \tag{32}$$

$$B = \frac{\mu NI}{2}\left(\frac{1}{\sqrt{4R^2 + L^2}}\right) \tag{33}$$

This equation describes the axial magnetic field strength at half the coil length and along the centerline of a solenoid coil, which is useful for many electromagnet applications. This is because the magnetic field lines at the exactly half the solenoid coil length are purely in the axial direction, with no component in the radial direction. Because of this, the axial component of the magnetic field at any point in the coil is greatest at the exactly half the solenoid coil length, no matter how far away it is from the z – axis centerline (B field is constant along any distance from centerline, r, at half coil length, L/2).

However, the inductance of a real, finite solenoid coil requires a far more involved analysis. In addition to the finite length of the coil, there are several physical phenomena that cause deviations from the ideal theory of infinite solenoid coils. In particular, for solenoid coils undergoing solely DC currents, the effects of mutual inductance and self-inductance are particularly non-negligible. These effects are primarily caused by (1) the small but non-negligible dimensions of the wire diameter and (2) the close proximity of nearby coil turns and their effects on the coupled electromotive force induced in the coil. [18] These effects can be more feasibly

analyzed if one models a finite coil with round wire as a current sheet. A current sheet coil is a theoretical solenoid constructed using infinitely thin conducting "tape" wound, in a single layer, with zero spacing between turns. The infinitesimally small inter-turn gap eliminates small-scale field nonuniformities that are typically hard to analyze in real coils. The magnetic field strength and inductance of this theoretical solenoid coil are equivalent to the infinite solenoid coil that was previously described. However, this model can be extended to coils of finite length, where nonuniformities in the magnetic field strength and real dimensions of wires become particularly non-negligible. [18]

The greatest correction to the inductance of a finite solenoid coil is described using the Nagaoka coefficient. This Nagaoka coefficient corrects for the magnetic-field non-uniformity that appears when the length of the coil becomes comparable to its diameter (i.e., when the coil is short). The Nagaoka coefficient multiplies the infinite coil inductance solution as shown in Eq. (34) The analytical solution for the Nagaoka coefficient k_L is given in Eq. (35), [18]

$$L = \frac{\mu N^2 A k_L}{L_c} \tag{34}$$

$$k_L = \frac{8R}{3\pi L}\left[\frac{2\kappa^2 - 1}{\kappa^3}E(\kappa) + \frac{1-\kappa^2}{\kappa^3}K(\kappa) - 1\right] \tag{35}$$

$$\kappa = \frac{2R}{\sqrt{4R^2 + L^2}} \tag{36}$$

where κ is given in Eq. (36), and $E(\kappa)$ and $K(\kappa)$ are complete elliptic integrals of the first and second kind respectively. The complete elliptic integrals have to be calculated from infinite series, so it is often necessary to obtain k_L through approximations of Eq. (35) or through graphical analysis. A plot of the solution for the Nagaoka coefficient is shown in Figure 9.

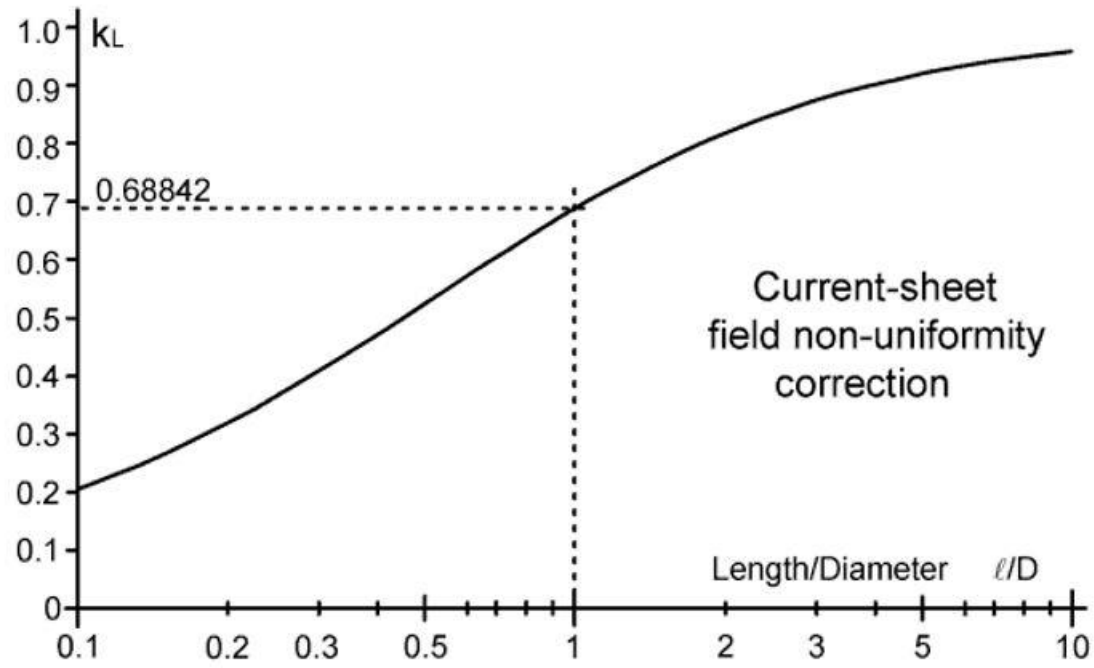

Figure 9. Plot of Nagaoka coefficient solution. [18]

The second set of correction factors account for the difference between real phenomena associated with a round-wire loop and the derived current sheet formulation. One correction factor, k_s, corrects for the difference between the self-inductance of a round-wire loop and that of a single-turn current sheet, while a second correction factor, k_m, corrects for the difference in the total mutual inductance of a set of round-wire loops as compared to that of a set of current-sheet loops. The solutions for these two correction factors are derived from empirical results and subsequent curve fit analyses have led to the equations given in Eq. (37) and Eq. (38) to solve for k_s and k_m, respectively. [18]

$$k_s = \frac{5}{4} - \ln\frac{2p}{d} \tag{37}$$

$$k_m = \ln 2\pi - \frac{3}{2} - \frac{\ln N}{6N} - \frac{0.3308}{N} - \frac{1}{120N^3} + \frac{1}{504N^5} - \frac{0.0012}{N^7} + \frac{0.0005}{N^9} \tag{38}$$

In conclusion, the final equation for a real, finite solenoid coil is given by Eq. (39). [18]

$$L = \frac{\mu\pi R_c^2 N^2}{L_c}\left[k_L - \frac{2L_c(k_m + k_c)}{\pi R_c N}\right] \tag{39}$$

This equation is essential for constructing a non-commercially available electromagnet intended for use as an inductor circuit element, as the transient solution for an LRC circuit is particularly sensitive to the inductance value of the inductor.

2.6 LRC Circuit Theory

An LRC series circuit is a closed loop circuit with a voltage source, capacitor, inductor, and resistor arranged in series. A diagram of an LRC circuit is shown in Figure 10.

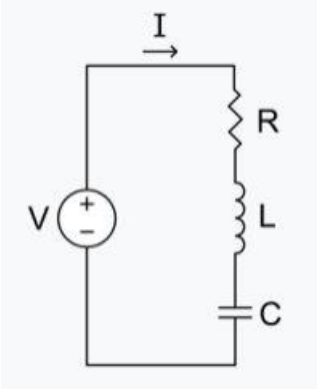

Figure 10. LRC series circuit schematic. [19]

The voltage source can either provide a DC or AC voltage output. For a DC voltage source output, the capacitors are charged until the voltage across the capacitors equals the voltage provided by the voltage source. While charging the circuit, the time of charge is dependent only on the capacitance of the capacitor and the resistance of the resistor. Therefore, charging an LRC circuit can be modeled as an RC circuit. A diagram of an RC circuit is shown in Figure 11.

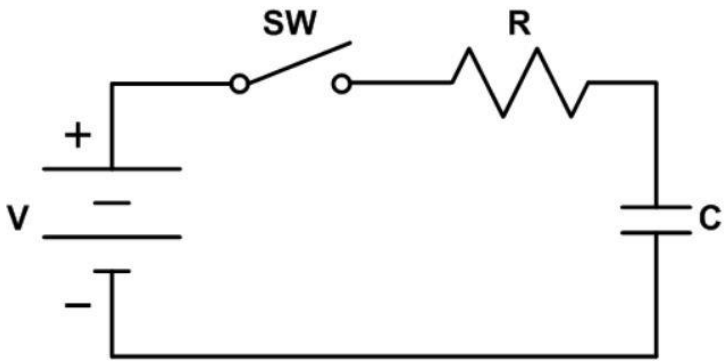

Figure 11. RC charging circuit schematic. [20]

The voltage across a resistor follows Ohm's Law, which is given in Eq. (40).

$$V_R = IR \tag{40}$$

Furthermore, the voltage across a capacitor with no initial charge is given by Eq. (41). 21]

$$V_c = \frac{1}{C}\int I(t)dt \tag{41}$$

Using Kirchhoff's voltage law (KVL, the governing equation for the voltage across the circuit elements in an RC circuit is given by Eq. (42). [21]

$$V_s - RI - V_C(t) = 0 \tag{42}$$

Substituting in Eq. (41) into Eq. (42) and taking the time derivative of both sides gives the differential equation in terms of the transient current response in Eq. (43).

$$R\frac{dI}{dt} + \frac{1}{C}I = 0 \tag{43}$$

Solving the differential equation, the current as a function of time in the RC circuit is given by Eq. (44).

$$I(t) = I_0 e^{-\frac{t}{RC}} = I_0 e^{-\frac{t}{\tau}} \tag{44}$$

Eq. (44) can be substituted into Eq. (42) using the initial conditions $V_C(0) = 0$ and $I(0) = \frac{V_S}{R}$ to give the transient response for the voltage across the capacitor during charging, given in Eq. (45). [21]

$$V_c(t) = V_s\left(1 - e^{-\frac{t}{RC}}\right) = V_s\left(1 - e^{-\frac{t}{\tau}}\right) \tag{45}$$

The time that it takes to fully charge the capacitor depends on the time constant τ given in Eq. (46).

$$\tau = RC \tag{46}$$

The time to charge the capacitor to within 2% of the voltage source is 4τ, as shown in the RC charging plot in Figure 12. Therefore, a resistor should be selected so that the time to charge is reasonable.

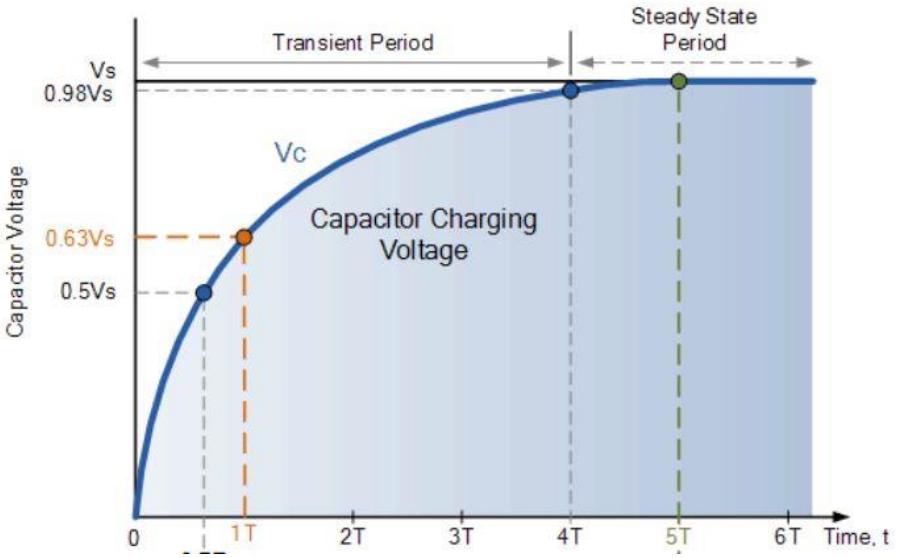

Figure 12. RC charging circuit voltage response. [21]

The voltage source can then be removed from the circuit once it has been used to charge the capacitor to the desired voltage. In this case, the LRC circuit is open until a switch is used to close the circuit and discharge the capacitor. The capacitor discharge transient response for the current is an important parameter that affects the fields produced in the electromagnet. The voltage across the electromagnet can be modeled as the voltage across an inductor and is given in Eq. (26). Using Kirchhoff's voltage law (KVL) and taking the first derivative of both sides with respect to time, the governing equation for the current in an LRC circuit is given by Eq. (47).

$$L\frac{dI^2}{dt^2} + R\frac{dI}{dt} + \frac{1}{C}I = 0 \tag{47}$$

This equation can be expressed in terms of the damping factor and natural frequency according to Eq. (48)

$$\frac{dI^2}{dt^2} + 2\alpha\frac{dI}{dt} + {\omega_0}^2 I = 0 \tag{48}$$

where the damping factor and natural frequency are given in Eq. (49) and Eq. (50), respectively.

$$\alpha = \frac{R}{2L} \tag{49}$$

$$\omega_0 = \frac{1}{\sqrt{LC}} \tag{50}$$

The damping ratio, ζ, is then defined in terms of the damping factor and natural frequency, as well as the circuit parameters, according to Eq. (51).

$$\zeta = \frac{\alpha}{\omega_0} = \frac{R}{2}\sqrt{\frac{C}{L}} \tag{51}$$

Solving the differential equation, the current as a function of time in the LRC circuit for the overdamped case is given by Eq. (52),

$$I(t) = A_1 e^{s_1 t} + A_2 e^{s_2 t} \tag{52}$$

where the roots of the differential equation are given in Eq. (53). [22]

$$s_{1,2} = \frac{-R \pm \sqrt{R^2 - 4\frac{L}{C}}}{2L} \tag{53}$$

To solve for the two coefficients A_1 and A_2, the two boundary conditions given in Eq. (54) and Eq. (55) must be used to give the complete solution for the discharge current as a function of time provided in Eq. (56). [22]

$$I(0^+) = I(0^-) = 0 \tag{54}$$

$$\frac{dI}{dt}(0^+) = \frac{V_s}{L} \tag{55}$$

$$I(t) = \frac{2V_s}{L}\left[e^{\left(\frac{-R+\sqrt{R^2-\frac{4L}{C}}}{2L}\right)t} - e^{\left(\frac{-R-\sqrt{R^2-\frac{4L}{C}}}{2L}\right)t}\right] \tag{56}$$

To achieve the electromagnetic separation of a model rocket's stage, the response of the LRC circuit must be overdamped. This is because an underdamped circuit would exhibit oscillatory behavior that would consequently switch the direction of the magnetic field inside the electromagnet. Therefore, the permanent magnet would continue to be pulled back into the electromagnet and the booster would fail to be detached from the rocket airframe. The system could theoretically be critically damped, however, minor deviations from the critically damped condition may result in a period of time where the system is underdamped. Therefore, it is

necessary to have a safety factor multiplying the ideal damping ratio to ensure the system is overdamped for the entire circuit discharge. For the response of the LRC circuit to be overdamped, the damping ratio must be greater than one so that the circuit parameters must satisfy the inequality given in Eq. (57).

$$R > \sqrt{\frac{4L}{C}} \tag{57}$$

The peak current during discharge is inversely proportional to the total resistance, which is the sum of the resistor resistance and the resistance in the wire, given by Eq. (58).

$$R = R_r + \frac{\rho_w L_w}{\pi r_w^2} \tag{58}$$

where ρ_w is the density of the material of the wire, L_w is the total length of the wire in the circuit, and r_2 is the radius of the wire cross-section. Therefore, to maximize the peak current, the resistor used in the LRC circuit must be minimized while still providing enough resistance to cause the response to be overdamped according to Eq. (57).

2.7 COMSOL and the Magnetic Field Module

COMSOL Multiphysics® is a finite element analysis (FEA) solver and simulation software that uses physics-based user interfaces and coupled systems of partial differential equations. [4] Using a one or more physics modules in COMSOL allows for coupling effects that are often not possible in most FEA software. In particular, the magnetic fields module can be used to solve for the magnetic field strength of permanent magnets and electromagnets with accuracy and detail that is difficult to be achieved by analytical results. In addition, COMSOL's extensive library of magnetic and ferromagnetic materials allows a variety of permanent magnet and electromagnet configurations to be quickly analyzed. The magnetic field module in COMSOL couples Ampere's Law with magnetic insulation and other user-specified boundary conditions. The three partial

differential equations that COMSOL couples to satisfy Ampere's Law are given in Eq. (59), Eq. (60), and Eq. (61),

$$\boldsymbol{\nabla} \times \boldsymbol{H} = \boldsymbol{J} \tag{59}$$

$$\boldsymbol{B} = \boldsymbol{\nabla} \times \boldsymbol{A} \tag{60}$$

$$\boldsymbol{J} = \sigma \boldsymbol{E} \tag{61}$$

where $\boldsymbol{J}$ is current density, $\boldsymbol{A}$ is magnetic vector potential, σ is electrical conductivity, and $\boldsymbol{E}$ is electric field intensity. [4] The magnetic insulation condition can be applied to the outer boundary of the control volume and the governing equation at the boundary is then given by Eq. (62).

$$\hat{\boldsymbol{n}} \times \boldsymbol{A} = 0 \tag{62}$$

For problems involving coils and electromagnets, coil physics can be applied to the domain of the coil wire geometry. The three vector equations that COMSOL uses to simulate coil physics are given by Eq. (63), Eq. (64), and Eq. (65),

$$\boldsymbol{J_e} = \frac{NI_{coil}}{A} \boldsymbol{e}_{coil} \tag{63}$$

$$\boldsymbol{B} = \mu_0 \mu_r \boldsymbol{H} \tag{64}$$

$$\boldsymbol{D} = \epsilon_0 \epsilon_r \boldsymbol{E} \tag{65}$$

where, ϵ_0 is the permittivity of a vacuum, ϵ_r is the relative permittivity, and $\boldsymbol{D}$ is the electric flux density. [4] To apply materials to the domains of a model involving the magnetic fields module, the electrical conductivity, relative permittivity, and relative permeability of all materials must be specified, even if certain materials (such as air from the COMSOL library) are not necessarily magnetic or conductive in nature.

Chapter 3: Methodology

3.1 Permanent Magnet Sizing and Selection

To size the permanent magnet, the first steps are to select the magnet material and geometry. Since the magnetic field strength at the surface of a permanent magnet is proportional to the residual magnetism property of the material, it is often most desirable to go with a material that maximizes this property value. A list of commercially available permanent magnet materials and their respective residual magnetism values are shown in Table 1.

Table 1. Permanent magnet material properties. [1]

Material	Residual Flux Density (Br) (Teslas)	Maximum Energy Product (MGOe)	Coercivity (KOe)	Maximum Working Temperature (C°)
Nd-Fe-B (sintered)	1.0 - 1.4	Up to 45	Up to 30	180
Nd-Fe-B (bonded)	0.2 - 0.6	Up to 10	Up to 11	150
Sm-Co (sintered)	0.8 - 1.1	Up to 30	Up to 25	350
Sm-Co (bonded)	0.4 - 0.8	Up to 12	Up to 10	150
Alnico	0.7 - 1.4	Up to 10	Up to 2	550
Hard Ferrite	0.2 - 0.4	Up to 4	Up to 3	300
Flexible	0.1 - 0.3	Up to 2	Up to 3	100

Ultimately, I chose sintered neodymium (Nd-Fe-B) because of its high residual magnetism value, wide availability, and low cost. A cylindrical geometry was then chosen because this geometry allowed for the best slip fit within the solenoid electromagnet core; furthermore, there are relatively simple analytical solutions for the force and magnetic field strength at the surface of a cylindrical magnet because of it flat end-surfaces and axisymmetric “dipole” distribution. The WARRIORS I and SPACEJAM MQP teams also chose this material and geometry for similar reasons and were relatively successful with its implementation in the electromagnet actuator. [1] [3]

To determine the required length and radius of the magnet, I also estimated the peak forces that the boosters experience during the rocket launch. If it is assumed that the permanent magnet has a slip fit with half of its length confined to the core of the electromagnet, then the strength of the electromagnet was hypothesized to be able to withstand the net axial force. Therefore, it was assumed that the axial forces were negligible compared to the structural integrity of the

electromagnet; thus, these forces were ignored for the purpose of magnet sizing. However, the two radial forces, asymmetric drag and spin centrifugal force, had to be considered to determine the adhesive force required between the electromagnet core and permanent magnet. These two forces can be calculated using Eq. (2) and Eq. (5), respectively. The sum of these two forces can then be equated to the force between two nearby magnetized surfaces given in Eq. (12). Substituting Eq. (20) for the magnetic field of a cylinder into this equation and using πR^2 for the cross-sectional area of a cylinder then gives Eq. (66).

$$\omega^2 r + \frac{1}{20}\rho v^2 C_d A = \frac{\pi B_r^2}{8\mu_0}\left(\frac{R_m^2 L_m^2}{R_m^2 + L_m^2}\right) \tag{66}$$

This force balance thus becomes dependent on both the radius and length of the cylindrical permanent magnet. These variables can then be optimized to give the smallest permanent magnet size required to provide the necessary adhesive force during launch. This was achieved by creating a 3D plot of force, radius, and length. Since the minimum force can be solved for analytically, the level curve corresponding to this force value can be isolated to be analyzed for the relationship between the radius and length of the permanent magnet. This can be done according to the MATLAB code provided in Appendix C. The values selected should primarily consider the length of the magnet, as the length must fit within the size constraints of the motor section of both the main rocket and booster. The radius and length sizing is also limited to commercially available permanent magnets. Since magnets are sized and manufactured with specific radius to length ratios, there will likely only be a select few sizings that will be optimal according to the force level-curve. Once a magnet has been selected, it would be wise to enter the magnet radius and length into Eq. (66) to ensure that the magnet adhesive force is greater than the peak forces experienced during launch.

3.2 Coil Design and Fabrication

Once the permanent magnet dimensions have been finalized and a permanent magnet has been selected, the electromagnetic coil can be designed to produce a great enough magnetic field to dissipate that of the permanent magnet. Eq. (20) for the magnetic field strength at the flat-end

surface of the cylindrical permanent magnet and Eq. (33) for the magnetic field strength along the center axis of the electromagnet can be equated according to Eq. (67) to solve for the required coil parameters.

$$\frac{B_r L_m}{\sqrt{R_m^2 + L_m^2}} = \frac{\mu N I}{\sqrt{4R_c^2 + L_c^2}} \tag{67}$$

This magnet field balance then becomes a function of the length, radius, number of turns and the current, where the required current is the only parameter that is not dictated by the coil design. For a single-layered coil, the maximum number of turns is a function of the length and the minimum possible pitch given by Eq. (68) and Eq. (69).

$$N_{max} = \frac{L_c}{p_{min}} \tag{68}$$

$$p_{min} = \frac{d}{\sqrt{1 - \left(\frac{d}{2\pi R_c}\right)^2}} \tag{69}$$

The length of the coil should be maximized to allow for the maximum number of turns. This depends on the space available in the motor section, so the length between the motor body tube and the inside of the main airframe must be measured. In addition, in order for the permanent magnet to have a slip fit within the solenoid coil, the radius of the coil must be approximately equal to that of the permanent magnet. Therefore, the coil radius is essentially fixed and was calculated using the magnet size optimization equation given in Eq. (66).

Another important consideration is the selection and sizing of the ferromagnetic core. The material used for the ferromagnetic core should have a high relative permeability because this will amplify the magnetic field for a given coil size. A steel core material was selected because of its high relative permeability, low cost, and wide availability. The radius of the steel core should be equal to that of the permanent magnet so that both fit within the tubing of the coil. The magnetic field strength would be maximized if the steel core length equaled the coil length; however, the

permanent magnet must have enough room within the coil as to not fall out during the rocket launch. Therefore, the core should be sized so that the combined permeability of the coil is sufficient to amplify the magnetic field while also allocating enough space in the coil for the permanent magnet. A simple, yet suitable, configuration for the coil core is to have the steel core section and permanent magnet each take up half of the coil's length. The combined permeability of the coil then is given by Eq. (70)

$$\mu = L_c\left(\frac{\mu_1\mu_2}{\mu_2 L_1 + \mu_1 L_2}\right) \tag{70}$$

Substituting this into Eq. (67) then gives the magnetic field strength balance with all unknowns solved for except current. The current can then be solved for in Eq. (71) to find the minimum current required during circuit discharge for a successful separation

$$I = \frac{B_r L_m}{\sqrt{R_m^2 + L_m^2}}\frac{\sqrt{4R_c^2 + L_c^2}}{NL_c}\left(\frac{\mu_2 L_1 + \mu_1 L_2}{\mu_1\mu_2}\right) \tag{71}$$

The prototype coils for circuit testing were made from magnetic copper wire, garolite tubing, epoxy, and a cardboard base. The garolite tubing ordered had a specified radius based on the optimized radius of the permanent magnet R_m, which I ultimately equated to the coil radius R_c. The garolite tubing was cut to the length specified by L_c while under a clamp. This tubing was then epoxied to a small cardboard base to serve as an end-holder while wrapping the turns of magnetic copper wire. This way, the wiring wouldn't unravel before the final coat of epoxy was applied. The wire was then wrapped around the garolite tubing starting from the end attached to the cardboard base. The wire was wrapped until the specified maximum number of turns N_{max} was achieved, ideally spanning the entire length of the tubing. A coat of epoxy was then spend over the wiring and let sit to harden for 1-2 hours. While the epoxy dried, the coil was placed under a clamp and the excess wiring was taped to a surface to secure the wiring to the tubing.

3.3 LRC Circuit Design

With the finalization of the coil parameters, the inductance of the electromagnet can be calculated using Eq. (39). The Nagaoka coefficient k_l then is determined by graphical analysis using the selected radius and length of the electromagnet. The correction factors k_s and k_m can be calculated using Eq. (37) and Eq. (38), respectively. This will give the inductance of the electromagnet as an inductor circuit element in the LRC series circuit. The voltage for charging the circuit was dependent on the power source that could be brought to the launch site, since the capacitors must be charged as part of the ground test required before launch. With the voltage and inductance of the circuit already determined, the transient solution for the circuit current during discharge is then dependent on the capacitance of the capacitor and the resistance of the resistor according to Eq. (58). The peak current increases with increasing capacitance and decreases with increasing current, so the resistors selected should be minimized so that the system is just overdamped. Another technique for optimizing the electromagnetic actuator system is to minimize the size of the capacitors. Large capacitors often take up a large section of the electronics bay and substantially increase the weight of the rocket, which decreases the maximum altitude attainable. Therefore, the capacitors should be sized with just enough capacitance to allow for the peak current to be greater than the minimum current for separation calculated from Eq. (71).

3.4 COMSOL Modeling and Simulations

The CAD model geometry was created using COMSOL's model builder capabilities. The coil core was modeled as two cylindrical bodies, each with length and radius based on those calculated in the coil design methodology. The coil wire model could have been achieved in several ways. I ultimately chose to model the wire as a cylindrical shell geometry around the core cylinders and use the circular homogenized multi-turn coil physics feature in the coil interface because of its simplicity. The thickness of the cylindrical shell was based off of the diameter of the magnetic copper wire being used for the circuit. A rectangular prism centered at the center of the coil was then created as a control volume so that the magnetic field would be computed throughout the volume. Figure 13 shows the assembly of the electromagnet geometry with numbered domains. Table 2 lists the numbered domains and shows the corresponding physics domain conditions and

materials that were applied to each domain. Table 3 lists each of the materials used and the properties needed for computation using the magnetic fields physics module.

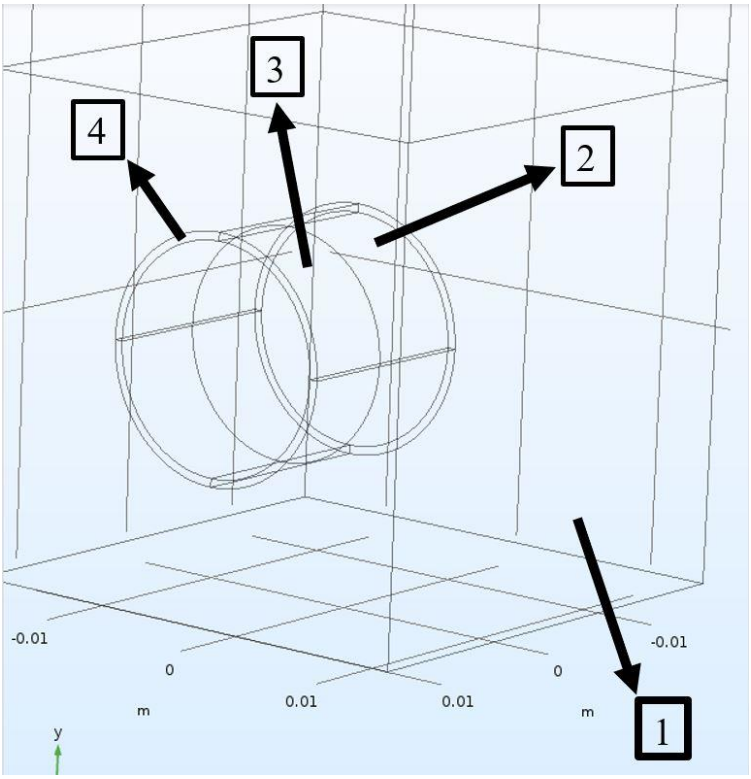

Figure 13. COMSOL coil model geometry and domain numbering.

Table 2. COMSOL coil model domain materials and conditions.

Domain	**Material**	**DC/AC Domain Condition**
1	Air	Magnetic Insulation Ampere's Law 3
2	Neodymium	Ampere's Law 2
3	Steel	Ampere's Law 1
4	Copper	Coil 1

Table 3. COMSOL coil model material properties.

Material	**Electrical Conductivity [S/m]**	**Relative Permeability [1]**	**Relative Permittivity [1]**
Air	0	1	1
Neodymium	-	1.05	1
Low Carbon Steel 1002	8.41	100	1
Copper	5.998e7	1	1

The magnetic fields physics module was used to apply Ampere's Law to all domains in the geometry. Magnetic insulation was applied to the outer boundary of the rectangular prism control volume domain. Initial values were all set to zero at t = 0. The coil applied physics was applied to the cylindrical shell domain. The current entered in the coil module was the calculated peak current for the optimized actuator. This value, as well as other specifications for the optimized coil parameters, were entered as global parameters given in detail in Table 4. A mesh was applied to the final geometry once all of the physics was applied. A time-dependent solver module was applied to the model since the current varied as a function of time during circuit discharge. This solver was the used to compute the magnetic field strength throughout the control volume for a time interval of $0 < t < 0.7$s.

Table 4. COMSOL coil model global parameters.

Variable	Description	Value	Units
I_coil	Peak LRC Discharge Current	13	A
N	Coil Number of Turns	10	Turns
AWG	Coil Wire Diameter Size	24	-

3.5 Circuit Assembly, Testing, and Analysis

An example of a fabricated coil that was used for testing is shown in Figure 14. respectively. In addition, the circuit test experimental setup is shown in Figure 15 and Figure 16. The way in which the mount would be integrated into the rocket is shown in detailed model of the SPACEJAM rocket given in Appendix D.

Figure 14. Fabricated solenoid coil with R/L = 1.

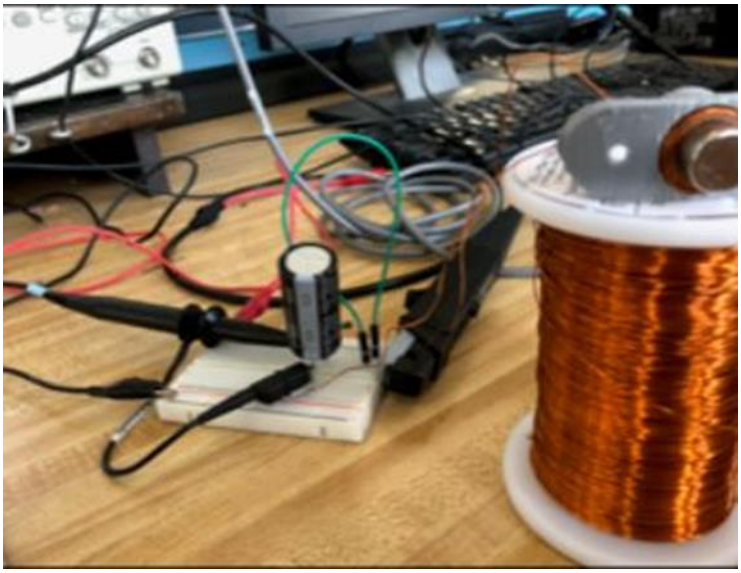

Figure 15. LRC circuit test and wiring.

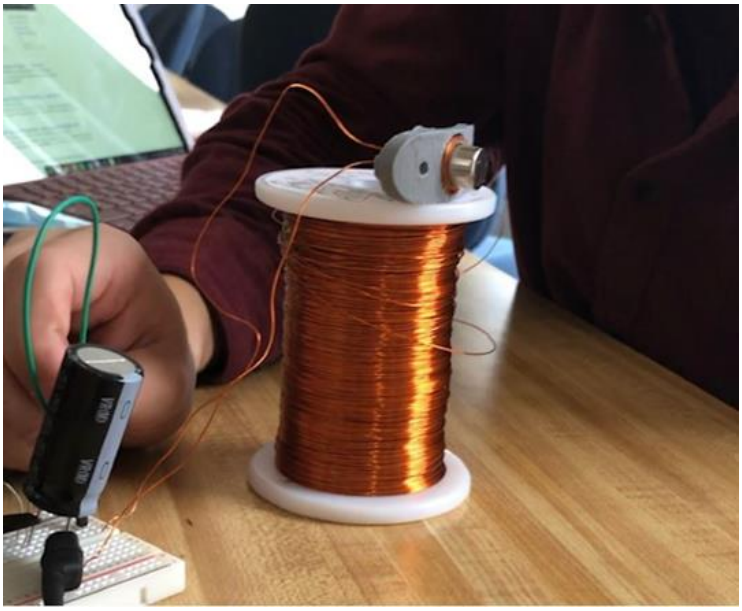

Figure 16. Actuator mount and wiring.

The circuit test used a known value of capacitance, resistance, and voltage, and used a coil that was fabricated specifically for the test. The coil was fabricated to have the maximum number of turns for its length and to have an equal radius to length ratio (R/L = 1) to analyze how close the Nagaoka coefficient can correct for the true inductance of real, finite coils. First, the capacitor was charged until the oscilloscope showed that the voltage difference across the capacitor was approximately equal to the power source voltage. Next, the circuit was opened so that the power source was no longer connected to the circuit. This was necessary because if the voltage source was still connected to the circuit during discharge, the power source would continually replenish the voltage difference across the capacitor and the current measurements would be disrupted. With the oscilloscope recording the current measurements, the circuit was then discharged so that the voltage across the capacitor approached zero. During the capacitor discharge, the electromagnet was observed to witness visible indications of the expected permanent magnet separation. The oscilloscope was also observed for the expected discharge current peak that was predicted according to theory. The discharge current plot generated by the oscilloscope was then downloaded as data points to be inputted into MATLAB. In MATLAB, this data was then analyzed using cftool, in which a custom equation in the form of Eq. (72) was curve-fitted to the data,

$$y(x) = a(e^{bx} - e^{cx}) + d \tag{72}$$

where a, b, c, and d are curve-fit coefficients solved using MATLAB's cftool. An equation in the form of Eq. (56) was attempted to be used in the curve fit, however, the solution for the curve-fit coefficients would not converge with this form. Instead, Eq. (72) had to be used. Once the curve-fit coefficients were computed, a MATLAB fsolve script was used to solve for the inductance. The curve-fit coefficients were set equal to what they would normally be in terms of circuit parameters according to Eq. (56) as a function of the unknown inductance L. The inductance value that was computed using the curve fit and fsolve was then compared to the inductance value that was obtained from the calculation based on electromagnetic theory using Eq. (39).

Chapter 4: Results

4.1 Permanent magnetic sizing and selection

From the Openrocket simulation, the estimated drag coefficient based on the booster geometry was found to be approximately 0.7. In addition, I estimated the maximum exhaust velocity of the rocket using the rocket path simulation program developed by the Controls team MQP, which was found to be approximately 275m/s. Furthermore, I used the atmospheric density at ground level, 1.225kg/m^3, as this was the maximum density possible during flight. I also calculated the frontal cross-sectional area of the booster airframe, 6.605e-4, assuming the diameter of the airframe was approximately equal to the diameter of an Aerotech F20 rocket motor (29mm).

This resulted with an estimated total outward radial net force of 7.34e-5N. To overcome these forces, the permanent magnet would have to be sized to produce an adhesive force at the surface greater than or equal to this value. The permanent magnet was sized using the MATLAB script given in Appendix C. A 3D surface curve of the permanent magnet force vs. the permanent magnet radius and length was generating in MATLAB and is shown in Figure 17.

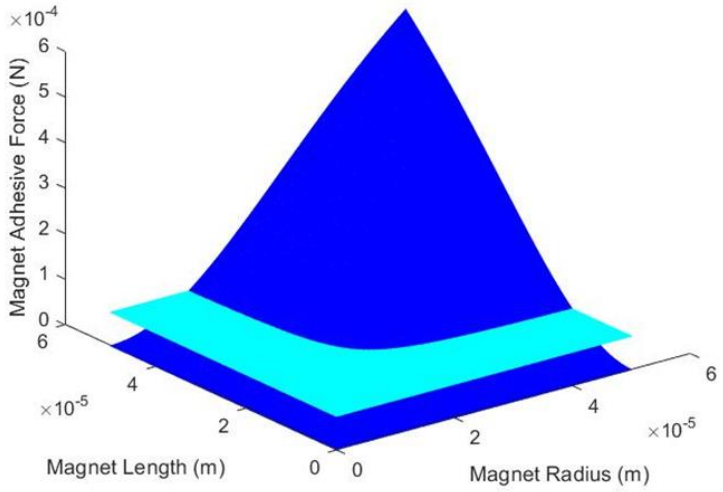

Figure 17. Permanent magnet 3D optimization.

The flat plane represents the intersection of the required permanent magnet force solution with the permanent magnet adhesive force as a function of radius and length. This intersection can then be translated to a 2D level curve which shows the possible combination of radius vs. length ratios that would satisfy the solution. Several examples of level curves corresponding to different solutions of the radial force balance equation are shown in Figure 18.

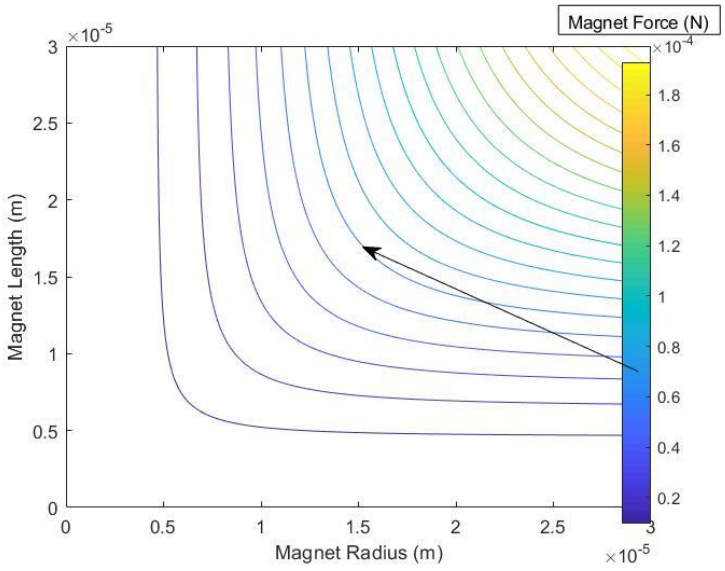

Figure 18. Permanent magnet optimization 2D level curves.

The level curve specified with an arrow corresponds to the solution that is shown in Figure 17. As seen from all of the example solutions, the optimal radius and length are equivalent to produce the maximum adhesive force. This in turn reduces the magnet volume, and thus magnet mass, which contributes to the lessened weight of the separation system and rocket weight as a whole. Even with a significant safety factor for the magnetic adhesive force, this permanent magnet sizing is quite small compared to that used by WARRIORS I and SPACEJAM. This is because they used a different equation for the cylindrical permanent magnet end-face adhesive force. This equation was given as an approximation with no supportive derivation, while the equation used for my calculation was based on fundamental magnetic theory. Thus, the WARRIORS I calculations led them to use oversized magnets for their separation system. This not only led to added mass for the permanent magnet, but also added mass from the large capacitors needed to create enough reversed magnetic field to counteract the large magnetic force produced by these large magnets.

4.2 Coil Design and Fabrication

Once the magnetic adhesive force required to counteract radial forces during launch was calculated, the next design calculations involved those for the optimal coil dimensions and design. Based on the restraints of using a mid-powered I motor, the coil length was restricted to be approximately 0.0063m. Based on the radius calculated from the permanent magnet optimization, the inner radius of the coil would have to be approximately 0.00635m. With this coil length, the maximum number of turns based on the minimum pitch possible for the wire diameter used was calculated to be 10 turns. Using a steel core and neodymium permanent magnet, each taking up half of the coil length, the effective relative permeability of the core was calculated to be 2.0782, which would be used for the calculation for the inductance of the coil. If the entire core were to have a steel core the effective relative permeability would be 100. The effective permeability of the SPACEJAM rocket, which attempted to considered the effects of a half steel core, used an effective relative permeability of 50, which was half the permeability on a full steel core. This showed that it is necessary to use Eq. (70) to efficiently calculate the effective permeability. This calculation can especially affect the inductance of the coil, as these parameters are linearly proportional to the effective permeability. Using the real, finite inductance equation given in Eq. (39), the inductance of the coil fabricated with these parameters would be 3.3565e-6H. Comparing this to the inductance calculated from Eq. (29) for an infinite coil, 5.1689e-6H, it is clear that it is necessary to use Eq. (39) for shorter, personally-fabricated coils. This is especially important when using this inductance value in the solution for an LRC circuit. Furthermore, using Eq. (71), the minimum current to exactly reverse the permanent magnet magnetic field was calculated to be 12.03A. Thus, this current must be achieved by the maximum current of the pulse produced by the LRC circuit.

4.3 LRC Circuit Design

Using a source voltage value of 32.4V, which was the maximum from available power sources, as well as an inductance value of 3.3565e-6H, the transient current solution for different sized capacitors is shown in Figure 19. The resistance values chosen for each capacitance case was that to minimize the resistance while still allowing the system to be overdamped, which allowed

the peak current of the transient solution to be maximized. Of these capacitance cases, the capacitor that would optimize the circuit by reaching just enough peak current to discharge the boosters would be the 10μF capacitor. Compared to the capacitance of the capacitors used for WARRIORS I and SPACEJAM, 13,300μF and 4,000μF respectively, this capacitance greatly reduces the size of the required capacitors. This, in turn, increases the space in the rocket's electronic bay, as well as reduces the overall mass of the rocket to increase the maximum altitude obtainable.

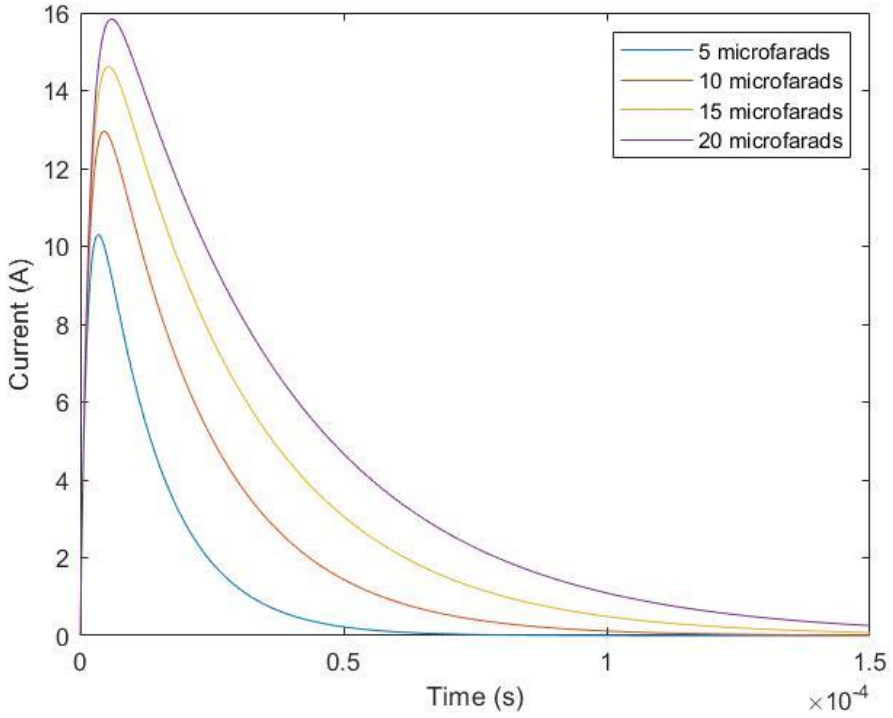

Figure 19. Transient current vs. time response for optimized capacitor range.

4.4 COMSOL Modeling and Simulations

The assembled COMSOL CAD model geometry with domain labels was given in Figure 13. This was constructed using two layers of cylinders, with the inside cylinder being divided into two equal length sections to represent the two core materials. The outer layer of the cylinder represented the wire turn layer, with a thickness equal to that for a 24 AWG wire diameter. The applied domain conditions and materials according to Table 2 and Table 3 were applied to this

geometry. A two-step solution, including a coil geometry analysis and a stationary solver, was conducted for this mesh and the specified applied physics to produce the final solution for the magnetic flux density shown in Figure 20.

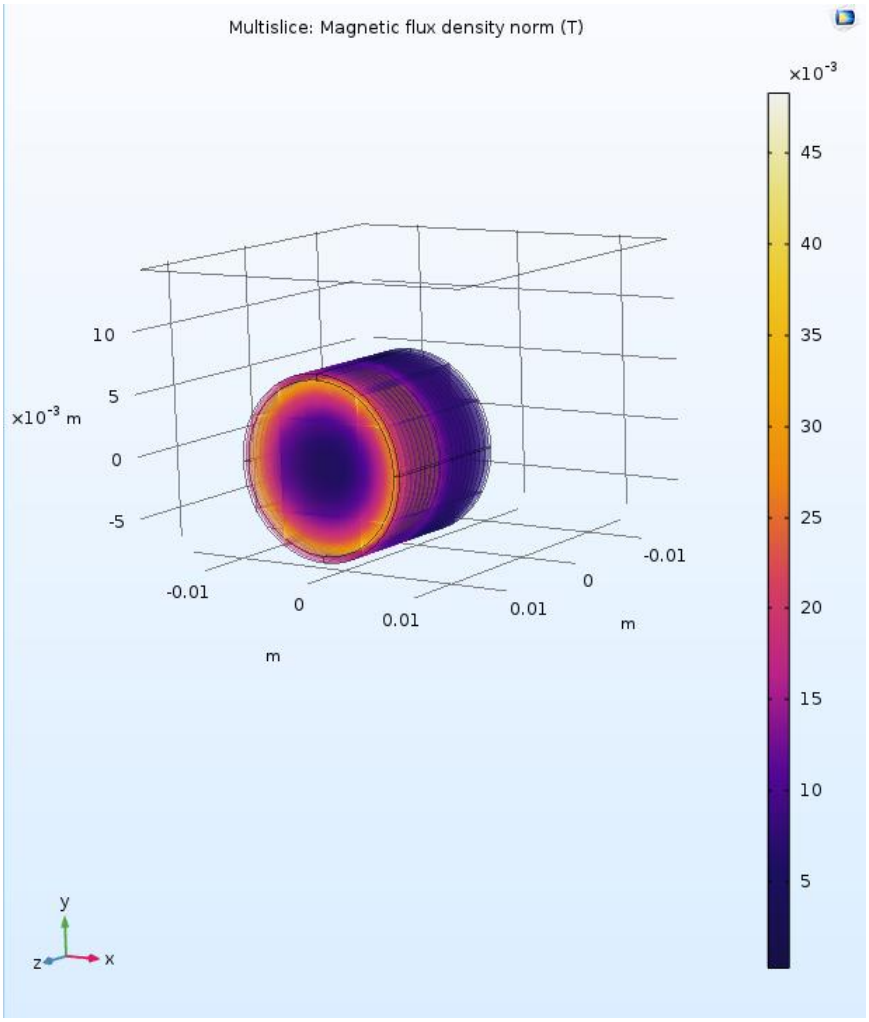

Figure 20. COMSOL magnetic flux density results.

The current used for this model was that for the theoretical peak current as shown in Figure 19 with a capacitance of 10μF. As seen from Figure 20, the magnetic flux density is both a function of the radial and axial component of the magnetic flux density. At the exact center of the coil, between the two core material sections, the magnetic flux density is purely in the axial direction according to the model and from the derived magnetic theory. Therefore, the axial magnetic field strength is a maximum at this center plane. Evaluating the magnetic flux density at this plane

produced a purely axial magnetic flux density of 0.0451T. This obtained value from the COMSOL model was much greater than the required magnetic field density for separation that was previously calculated, 0.0176T. Therefore, the results show that according to the COMSOL model computations, the fabricated electromagnet produces far more than enough magnetic field density than was required, and consequently, this fabricated electromagnet will hopefully produce enough magnetic flux density to counteract the magnetic field of the permanent magnet to allow for a successful booster separation during an actual launch test.

4.5 Circuit Assembly, Testing, and Analysis

Using the experimental setup described in the methodology, the oscilloscope gave a plot for the discharge current and voltage across the capacitor as shown in Figure 21. These plots highly resemble that of the expected theory, as the voltage across the capacitor drops from the source voltage to zero and the current immediately peaks and then settles to zero as the capacitor voltage zeros out. Isolating the current pulse data points from Figure 21 and plotting the data points in MATLAB gave the current plot shown in Figure 22. This was then compared to the plotted theoretical current pulse shown in Figure 23.

Figure 21. Oscilloscope transient response of LRC circuit from circuit testing.

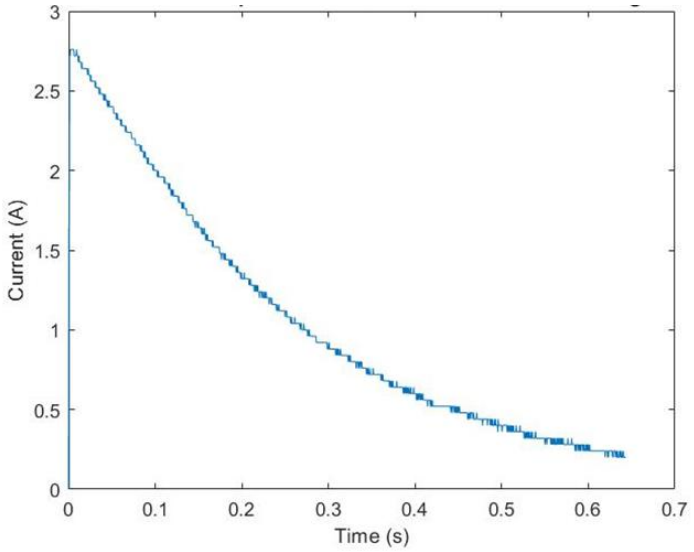

Figure 22. Transient response of LRC circuit from circuit testing.

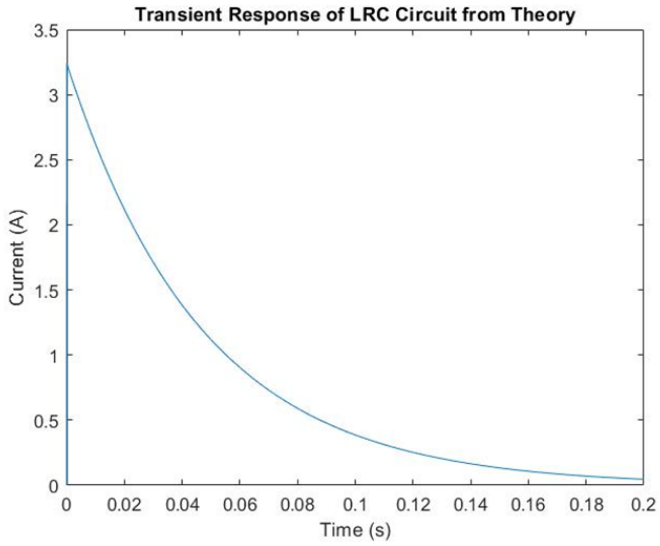

Figure 23. Transient response of LRC circuit from theory.

As seen from these two figures, the measured current plot of the measured current data highly resembles that of the theoretical current plot. The respective peak currents for the measured and theoretical current plots are 2.76A and 3.24A, respectively. These are within 14.8% of each other, indicating a significant improvement in accuracy compared to the test results of WARRIORS I and SPACEJAM. The measure transient current plot was also analyzed using the cftool in MATLAB and a curve fit was generated according to Figure 24.

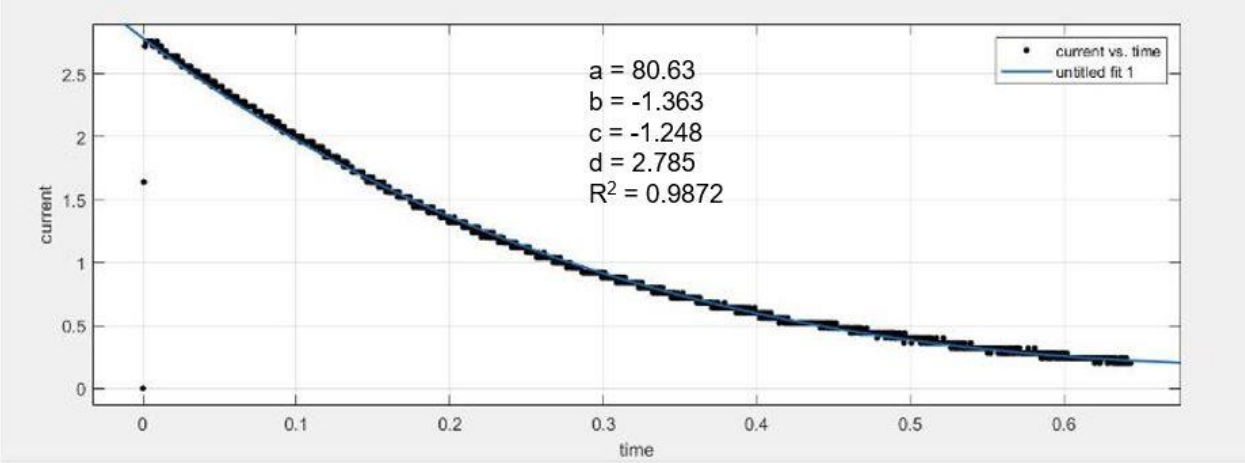

Figure 24. Transient response of LRC circuit test curve fitting.

As shown from the plot, the curve fit accurately resembles that of the derived transient solution with a given R^2 of 0.9872. This curve plot required the theoretical transient solution to be simplified to simple coefficients as a function of the inductance, L. The computed curve-fit coefficients were then equated to the transient current solution to provide a system of three equations as a function of inductance, L. This system of equations is shown in an fsolve function in MATLAB as given in Appendix C. The solution to this code was then evaluated to solve for the inductance of the fabricated coil. The resulting curve fit inductance value was computed to be 3.1052e-6H, compared to the calculated value of 3.3565e-6H. This shows a percent error of 7.4870%, indicating a quite accurate approximation according to the real, finite coil theory.

Chapter 5: Conclusions

This project investigated the feasibility of designing, fabricating and testing an electromagnetic actuator. From magnetic theory of a permanent magnet, electromagnetic of a closed-core solenoid coil, and LRC circuit theory, this actuator was sized and optimized to provide enough force to successfully eject the boosters while minimizing the mass of several actuator components. In particular, I showed that the minimum required capacitors for the actuator circuit are significantly smaller and less powerful than those used in previous booster separation designs. In addition, the permanent magnet was appropriately sized to provide a large enough adhesive force during launch. The permanent magnet dimensions were also optimized to minimize the mass of the magnet and reduce the power requirements of the LRC circuit. As shown in the results section, the COMSOL model, which was based on the calculated coil dimensions and parameters, was solved for the magnetic flux density within the electromagnet using a stationary solver. The results of this analysis showed that the magnetic flux density at the center of the coil was more than adequate for a successful booster separation according to the derived theory. This confirms the the accuracy of the derived equations for the magnetic flux density and effective permeability based on basic principles, which hadn't been adequately derived and provided in past rocket MQP projects. Furthermore, the transient current solution derived for an LRC circuit was proven to accurately model the response of the circuit test. The peak currents for both the calculated and the measured current plots were approximately equal. Also, the current curves closely paralleled each other, with small differences in the amount of damping. The successful curve fit on the measured current plot also showed that the derived solution for the transient current is a good model for the real-life response.

Given more time, fully integrating the system onto a prototype booster would have been the next goal. There was not enough time to continue testing the prototype of the electromagnetic system. Ultimately, actual testing during rocket flight would prove the capabilities of this system. Since the electromagnetic system was not flight ready by the scheduled launch for the SPACEJAM rocket, the system was not able to be detested on-board. With these solutions, I hope to provide future rocket MQP projects, as well as model rocket projects of other universities, with the confidence of using this separation system in their design. As for future model rocket projects,

there are many incentives for further analysis and full-scale rocket testing of this electromagnetic parallel separation system.

Chapter 6: Future Work

As previously mentioned, a major area of future work on electromagnetic booster separation is integration and testing with a full-scale model rocket and booster. The circuit tests conducted in this project only considered the ejection of a permanent magnet from the solenoid core, with a custom mount 3D printed for potential integration into a rocket airframe. However, these tests did not consider the weight of the booster, which adds inertia and potential friction to the system. Therefore, there is still some uncertainty whether the system would still work with the added mass and friction associated with the booster airframe and motor. Extensive ground testing, using an integrated separation system within a full-scale model rocket and booster setup, would significantly increase confidence in the compatibility and reliability of an electromagnetic booster separation system.

In addition, there has been little to no recent testing of an on-board computer signaling the LRC circuit to activate. This component of the overall separation system is a major requirement if a project team wishes to use this separation system in an actual model rocket launch. There are guidelines for creating this system using a MOSFET (metal-oxide semiconductor field-effect transistor) as a switch to close the LRC circuit when a signal is sent from the on-board computer. A full-scale construction and testing of this system with the electromagnetic actuator would be an essential next step before a launch test. The final goal would be to have successful booster ejections from the rocket airframe using the on-board computer signal and electromagnetic actuator during a model rocket test flight.

As a final remark on the potential advancements of electromagnetic booster separation, there are also further precautions that can be taken to ensure a successful booster separation. In particular, because the roll rate for typical model rockets can only be estimated, there are concerns that the rocket fins may be rotating fast enough to collide with the boosters as they are ejected. This, in turn, would create a major disturbance in the stability of the rocket and possibly lead to an ultimate rocket crash. As a safety precaution to minimize the risk for this happening, the force on the boosters during ejection could be increased to allow for a greater ejection acceleration. To accomplish this, the magnetic field strength at the center of the coil would have to be increased, meaning that the peak current during capacitor discharge would need to be increased. The easiest

way to increase the peak current would be to use capacitors with higher capacitance, as well as using the lowest resistor resistance possible without causing the system to be underdamped. If a test could be conducted to simulate a high enough roll rate as a ground test, this potential hazard can be identified and mitigated before an actual rocket launch.

References

1. Belliss, M., Brayshaw, P., Matook, G., Otterman, A., Sanchez-Torres, A., Moore K., Stechmann, D., Braun, T., JB3-RCK1, "WPI AIAA Research Rocket for the Investigation and Observation of Recovery and Staging (WARRIORS 1)," WPI Major Qualifying Project (MQP) report # JB3-RCK1, May 2006.

2. Buhler, J., Coverstone, T., Cummings, N., Fleming, S., Huleatt, T., McDonald, T., Renaud, P., Yocum, M, "WPI AIAA Research Rocket for the Investigation and Observation of Recovery and Staging (WARRIORS 2)," WPI Major Qualifying Project (MQP) report # JB3-RCK3, May 2008.

3. Furter, J., Halfrey, S., Handy, M., Legere, V., Lucena Farias, N., Murphy, C., Songer, N., and Tavares, J. JB3-1901, "Design and Integration of a High-Powered Model Rocket-III," WPI Major Qualifying Project (MQP) report # JB3-1901, May 2019.

4. "Understand, predict, and optimize physics-based designs and processes with COMSOL Multiphysics® Software [online] 2019. COMSOL, Inc. 2019. Available from: https://www.comsol.com/comsol-multiphysics. Accessed 3/20/2019.

5. Stine GH, Stine B. *Handbook of Model Rocketry*. 7th ed. Wiley; 2004.

6. Benso, T. Parallel Staging of a Booster [online] NASA 2019. Available from: https://spaceflightsystems.grc.nasa.gov/education/rocket/rktstage.html. Accessed 1/29/2019.

7. Sarradet, T. "Reloadable composite rocket motor diagram" [online] 2009. Available from: https://slideplayer.com/slide/4406026/. Accessed 2/3/2019.

8. “AeroTech announces Economax” [online] 2014. RCS Rocket Motor Components, Inc. Available from: http://www.aerotech-rocketry.com/news.aspx?y=2014. Accessed 3/15/2019.

9. “Rocket Rotations Body Axes” [online] 2018. NASA. Available from: https://www.grc.nasa.gov/www/k-12/rocket/rotations.html. Accessed 3/15/2019.

10. Griffiths, D.J. *Introduction to Electrodynamics*. 4th ed. Pearson. 1989.

11. Matthews, P.C. *Vector Calculus*. 1st ed. Springer-Verlag London. 1998.

12. “Holding strength parallel to the contact surface: shear force / moving force” [online] 2018. Supermagnete. Available from: https://www.supermagnete.de/eng/faq/Why-does-my-magnet-not-carry-the-maximum-weight-on-the-wall#holding-strength-parallel-to-the-contact-surface-shear-force-moving-force. Accessed 3/15/2019.

13. J. M. Camacho and V. Sosa. *Alternative method to calculate the magnetic field of permanent magnets with azimuthal symmetry*. Jan. 8, 2013. Available from: https://www.researchgate.net/publication/262707508_Alternative_method_to_calculate_the_magnetic_field_of_permanent_magnets_with_azimuthal_symmetry.

14. “Magnetic Fields Produced by Currents: Ampere’s Law” [online] 2019. BCcampus. Available from: https://opentextbc.ca/physicstestbook2/chapter/magnetic-fields-produced-by-currents-amperes-law/. Accessed 3/29/2019.

15. Laplante, P.A. (1999). *Comprehensive Dictionary of Electrical Engineering.* Springer-Berlin Heidelberg.

16. “Magnetic field inside finite solenoid” [online] 2019. StackExchange Physics. Available from: https://physics.stackexchange.com/questions/113232/magnetic-field-inside-finite-solenoid. Accessed 3/15/2019.

17. “Sources of Magnetic Fields” [online] 2019. MIT. Available from: http://web.mit.edu/8.02t/www/802TEAL3D/visualizations/coursenotes/modules/guide09.pdf.Accessed 4/14/2019.

18. D. W. Knight. An introduction to the art of Solenoid Inductance Calculation With emphasis on radio-frequency applications. Feb. 4, 2015. Available from: http://www.g3ynh.info/zdocs/magnetics/Solenoids.pdf

19. Wikiversity. Dec. 27, 2018. https://en.wikiversity.org/wiki/RLC_circuit

20. Jonathan, P. “Energy Loss Incurred when Charging a Capacitor in a RC Circuit” [online] Aug. 12, 2017. Available from: https://www.theknowledgeroundtable.com/tutorials/energy-loss-incurred-when-charging-a-capacitor-in-a-rc-circuit/. Accessed 4/15/2019.

21. “RC Charging Circuit” [online] 2019. Electronic-Tutorials. Available from: https://www.electronics-tutorials.ws/rc/rc_1.html. Accessed 4/15/2019.

22. McAllister W. “RLC natural response - derivation: A formal derivation of the natural response of the RLC circuit. 2017. Khan Academy. Available from: https://www.khanacademy.org/science/electrical-engineering/ee-circuit-analysis-topic/ee-natural-and-forced-response/a/ee-rlc-natural-response-derivation. Accessed 4/15/2019.

23. Cooper, C., Dings, D., Dohn, P., Fennick, J., Foster, K., George, E., Lapierre, N., Moquin, T., NAG-1901, “Design and Integration of a High-Powered Model Rocket-I,” WPI Major Qualifying Project (MQP) report # NAG-1901, May 2019.

Appendix A: AeroTech F20 Rocket Motor Statistics

AeroTech F20

Manufacturer:	AeroTech
Entered:	May 25, 2006
Last Updated:	Apr 16, 2019
Mfr. Designation:	F20W/L
Common Name:	F20
Motor Type:	SU
Delays:	4,7
Diameter:	29.0mm
Length:	8.3cm
Total Weight:	80g
Prop. Weight:	30g
Cert. Org.:	National Association of Rocketry
Cert. Date:	Sep 4, 2005
Average Thrust:	20.8N
Maximum Thrust:	40.3N
Total impulse:	51.8Ns
Burn Time:	2.5s
Propellant Info:	White Lightning
Data Sheet:	link
Availability:	regular

Appendix B: OpenRocket Simulator Geometry for SPACEJAM Rocket [23]

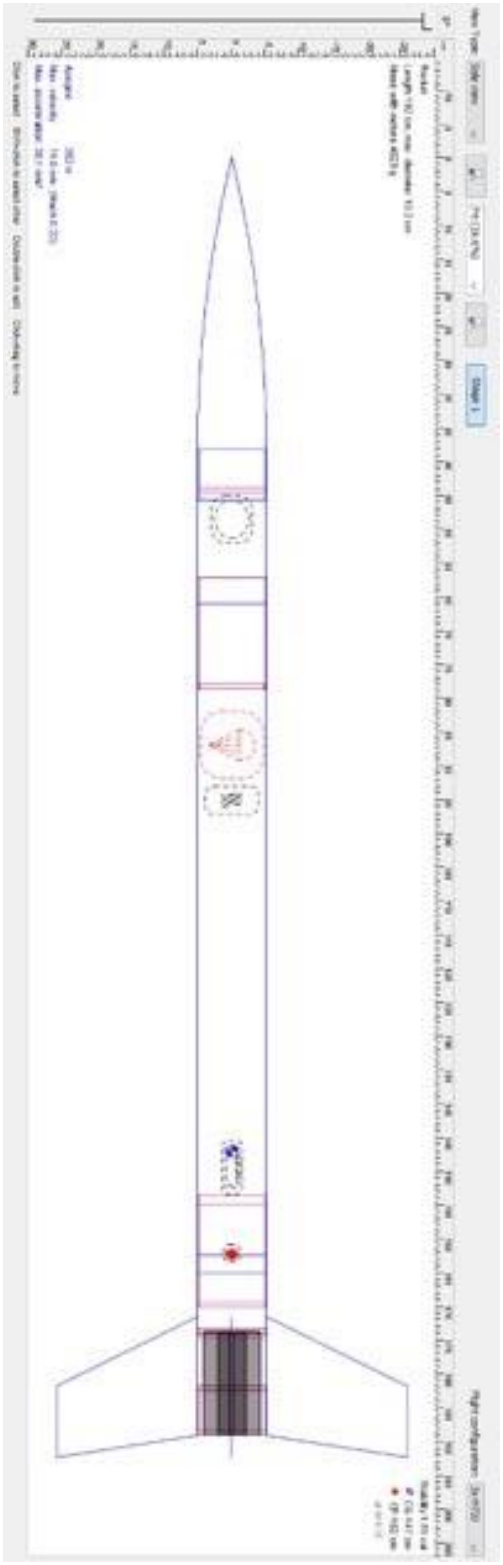

Appendix C: Electromagnetic Actuator Optimization MATLAB Code

```
clear all; clc; close all;

%% Magnet Parameters

omega = 62.8; %rad/s
r = 0.0653; %Distance from center of airframe to center of booster
rho  = 1.225; %kg/m^3
v = 275; %m/s
Cd = 0.7;
A = 6.605*10^-4; %m^2
Br = 1.2;
mu0 = 4*pi*10^-7;
mb = 0.12; %mass of booster, kg


%% Determine Lm and Rm from level curve of 3D plot of Bm vs. (Lm and Rm)


F1 = (omega^2*r*mb + 1/20*rho*v^2*Cd*A)*8*mu0/(pi*Br^2);
F1_matrix = F1*ones(301);

[Rm,Lm] = meshgrid(0:0.0000001:0.00003);
F2 = pi*Br^2/(8*mu0)*(Rm.^2.*Lm.^2./(Rm.^2+Lm.^2));

figure;
plot3(Rm,Lm,F1_matrix,'c',Rm,Lm,F2,'b')

figure;
contour (Rm,Lm,F2,20)

```

```
%% Coil Parameters

Rc = 0.0063;
Lc = 0.0063; %Estimate based on available length between motor body tube and airframe
L1 = Lc/2;
L2 = Lc/2;
d = 0.5106*10^(-3); %24 AWG wire diameter in meters
N = 10; %Calculate as one less than N_max
p = Lc/N;
mu1 = 1.05*mu0; %Neodyminum
mu2 = 100*mu0; %Steel
mu = Lc*mu1*mu2/(mu2*L1+mu1*L2);
mu_prime = 2*mu1*mu2/(mu1+mu2);
mu_r_eff = mu_prime/mu0
N_max = (Lc/d)*sqrt(1-(d/(2*pi*Rc)^2));

Rm = 0.00635;
Lm = 0.0127;

I_min = ((Br*Lm)/sqrt(Rm^2+Lm^2))*sqrt((4*Rc^2+Lc^2 ))/(N*mu2);

Bz = mu*N*I_min/2*(1/sqrt(Rc^2+Lc^2));
```

```
%% Inductance

k_l = 0.68842; %0.68842 for L/D ratio of 1
k_s = 5/4 - log(2*p/d);
k_m = log(2*pi) - 3/2 - log(N)/(6*N) - 0.3308/N - 1/(120*N^3) + 1/(N^5) - 0.0012/(N^7)

L = mu_prime*pi*Rc^2*N^2/Lc*(k_l - 2*Lc*(k_m+k_s)/(pi*Rc*N));
```

```
%% LRC Circuit Test

Vs = 32.4; %Voltage of power source
R = 10;
C = 4700*10^(-6);
R_overdamped = 2*sqrt(L/C); %Minimum resistance for given capacitor and coil


p1 = -R/(2*L) + sqrt(((R/(2*L))^2)-1/(C*L));
p2 = -R/(2*L) - sqrt(((R/(2*L))^2)-1/(C*L));


t = [0:0.0000001:0.00015];

I = Vs./L*(1./(p1-p2).*exp(p1.*t)+1./(p2-p1).*exp(p2.*t));

plot(t,I);

I_max = max(I);
```

```
87      %% Current vs. Capacitance Plot
88
89 -    for C = [5 10 15 20]*10^(-6);
90 -    R_min = 2.*sqrt(L./C)+1;
91
92 -    p1 = -R_min./(2.*L) + sqrt(((R_min./(2.*L)).^2)-1./(C.*L));
93 -    p2 = -R_min./(2.*L) - sqrt(((R_min./(2.*L)).^2)-1./(C.*L));
94
95 -    I = Vs./L*(1./(p1-p2).*exp(p1.*t)+1./(p2-p1).*exp(p2.*t));
96
97 -    plot(t,I)
98 -    hold on
99 -    end
```

```
101     %% Circuit Testing Curve Fit
102
103 -   data = (PHMQPCircuitTestCurrentData.Variables);
104
105 -   time = data(:,1);
106 -   current = data(:,2);
107
108 -   figure;
109 -   plot(t,I)
110
111 -   figure;
112 -   plot(time,current)
113
114     cftool
115
116     %a*(exp(b*x)-exp(c*x) + d %Form of curve fit solution
117
118 -   L0 = 0.00003674; %Initial guess
119
120 -   L_measured = fsolve(@inductance_solve,L0);
```

Appendix D: Electromagnetic Actuator Mount Connection in SPACEJAM Rocket [23]